International Journal of Plasticity 143 (2021) 103031

Contents lists available at ScienceDirect

International Journal of Plasticity

journal homepage: www.elsevier.com/locate/ijplas

A crystal plasticity finite element model embedding strain-rate sensitivities inherent to deformation mechanisms: Application to alloy AZ31

William G. Feather [a], Daniel J. Savage [a,b], Marko Knezevic [a,*]

[a] Department of Mechanical Engineering, University of New Hampshire, Durham, NH, 03824, USA
[b] Materials Science and Technology Division, Los Alamos National Laboratory, Los Alamos, NM, 87544, USA

ARTICLE INFO

Keywords:
A. Microstructures
B. elastic-viscoplastic material
B. rate-dependent material
B. Crystal plasticity
C. Finite elements
T-CPFE UMAT

ABSTRACT

The fundamental power-law relationship representing the flow rule in crystal visco-plasticity ensures uniqueness in the selection of slip systems accommodating imposed plastic strain-rates. The power-law relationship also introduces an artificially high strain-rate sensitivity in crystal plasticity simulations, unless a high value of the power-law exponent is used. However, the use of high values for the exponent is limited by numerical tractability. This paper presents a numerical method implemented in a crystal plasticity finite element (CPFE) model for embedding any value of the power-law exponent reflecting the true material strain-rate sensitivity. Importantly, the method does not increase computation time involved in the simulations. The enhanced CPFE model is used to interpret and predict a complex strain-rate sensitive response and microstructural evolution of AZ31 Mg alloy. Measured values of strain-rate sensitivity for slip and twinning modes are used in the simulations. Calculations show that the model successfully captures the phenomena pertaining to the effect of changing applied strain-rate on the mechanical response including flow stress and evolution of texture and twinning for a broad range of strain-rates ranging from 10^{-3} s^{-1} to 10^{3} s^{-1} and loading orientations in tension and compression. It is shown that such predictions are a consequence of not only relative amounts of slip and twinning activities driven by a set of accurately characterized hardening law parameters but also values of the strain-rate sensitivities inherent to individual deformation mechanisms. Besides, the model validates the measured strain-rate dependency of deformation mechanisms while accurately reproducing the mechanical data. Hence, the model can be used to verify and further refine or infer measured strain-rate sensitivity per deformation mechanism by reproducing experimental data.

1. Introduction

The overall constitutive behavior of polycrystals stems from the collective deformation behavior of constituent crystals/grains having local crystal orientation, size, and shape (Kocks et al., 1998). The relationship between the local deformation behavior at the grain-level and that of the polycrystalline aggregate is established using homogenization schemes. To this end, the mean-field (e.g. the Taylor-type or self-consistent (SC)-type (Feng et al., 2021; Ghorbanpour et al., 2017, 2020a; Lebensohn and Tomé, 1993; Riyad et al.,

---

[*] Corresponding author.
E-mail address: marko.knezevic@unh.edu (M. Knezevic).

https://doi.org/10.1016/j.ijplas.2021.103031
Received 4 October 2020; Received in revised form 8 April 2021; Accepted 13 May 2021
Available online 21 May 2021

2021; Schmidt et al., 2021; Tam et al., 2020; Wu et al., 2007a; Zecevic and Knezevic, 2015; Zecevic et al., 2016b)) and the full-field (e.g. the crystal plasticity finite element (CPFE)-type or Green's function fast Fourier transform (FFT)-type (Eghtesad et al., 2020; Eghtesad and Knezevic, 2020; Kalidindi et al., 1992; Lebensohn et al., 2012; Paramatmuni and Kanjarla, 2019)) theories are used. The mean-field models are more computationally efficient, while the full-field models are more accurate because they account for local grain-to-grain interactions. An important advantage of the mean-field models is their ability to efficiently handle the crystal lattice reorientation associated with deformation twinning. Several approaches have been developed in the literature for the modeling of twinning within the mean-field models like the predominant twin reorientation model (Tomé et al., 1991; Van Houtte, 1978), total Lagrangian model (Fast et al., 2008; Kalidindi, 1998; Kalidindi et al., 2006; Wu et al., 2007a, 2007b), and composite-grain (CG) model (Barrett et al., 2020; Proust et al., 2007). In contrast, modeling twin lamellae as discrete domains in spatially resolved full-field models has been attempted only recently (Ardeljan et al., 2015b, 2017; Ardeljan and Knezevic, 2018; Knezevic et al., 2016a; Kumar et al., 2015). However, such models have been primarily used for understanding of the mechanical fields associated with twin lamellae formation rather than for modeling of large plastic deformation of polycrystals (Knezevic et al., 2015).

In the CPFE-type models, a material point can embed a single crystal (Ardeljan et al., 2014, 2015a; Barrett et al., 2018; Diard et al., 2005; Fernández et al., 2013; Staroselsky and Anand, 2003) or a polycrystal whose response is obtained by a homogenization scheme. Formulations for the latter approach generally embed either SC models (Barrett and Knezevic, 2019; Segurado et al., 2012; Zecevic et al., 2017; Zecevic and Knezevic, 2017, 2019) or Taylor models (Ardeljan et al., 2016) at FE integration points. Accordingly, these multi-level models combine the two theories i.e. the FE full-field mechanics technique at a higher level and a mean-field technique at a lower level into a single approach, which takes advantage of both the computational speed of the mean field theories and the accuracy afforded by relaxing homogenization assumptions. In the present work, we adopt the modeling approach incorporating the Taylor-type model at each FE integration point developed in (Ardeljan et al., 2016) and later used in (Feather et al., 2019). The combined multi-level model is referred to as T-CPFE. Importantly, the modeling approach relaxes the iso-strain constraint assumption of the Taylor-type model formulation imposed over the entire polycrystal. Since the polycrystal is distributed over finite elements (i.e. FE integration points), the FE solver interrogates every sub-polycrystal as a separate Taylor-type model at every integration point with an imposed deformation gradient. As the deformation gradient varies spatially based on boundary conditions imposed over the FE mesh, the iso-strain constraint intrinsic to Taylor-type models is relaxed. While the iso-strain constraint assumptions is imposed over the sub-polycrystal embedded at an FE integration point, it is relaxed at the level of the entire polycrystal spanning over the entire FE mesh. The T-CPFE model at the grain-level incorporates the advanced CG twinning model while retaining the original Lagrangian numerical scheme. The twinning model allows multiple twin variants to form per grain. Finally, the model incorporates a dislocation density-based (DD) hardening law for the evolution of slip and twin resistances.

In this paper, the T-CPFE model is advanced to make deformation mechanism-level strain-rate sensitivities computationally feasible, thereby enabling the rate sensitivity behavior of alloy AZ31 to be modeled over a wide range of strain-rates. Since the alloy has a hexagonal closed packed (HCP) crystal structure and activation stresses vary between deformation modes, its deformation behavior is highly anisotropic (Akhtar, 1973; Alam et al., 2020; Becker and Lloyd, 2016; Ghorbanpour et al., 2019a, b; Kabirian et al., 2015; Knezevic et al., 2021; Partridge, 1967; Yoo, 1981). The plasticity in the alloy is carried out by a combination of crystallographic slip (basal, prismatic, and pyramidal slip modes) and deformation twinning (extension and contraction twinning modes). Activation stresses for these modes depend on strain-rate and temperature (Akhtar, 1975; Akhtar and Teghtsoonian, 1969) and highly varies across the modes inducing strong plastic anisotropy with texture (Ishikawa et al., 2005; Khan et al., 2011; Pandey et al., 2015; Watanabe and Ishikawa, 2009). Moreover, activity of deformation modes varies with loading paths. As a consequence of such variation, a sheet of AZ31 exhibits strong strain-rate sensitivity during in-plane tension and through-thickness compression, while approximately no strain-rate sensitivity during initial straining in-plane compression. The underlying reason is slip dominated deformation in the former cases and extension twin-dominated deformation in the latter case (Khan et al., 2011; Kurukuri et al., 2014; Wang et al., 2021). At higher strain levels, the strain-rate sensitivity for in-plane compression increases due to activation of the multiple slip modes. Such observations reveal that basic deformation mechanisms exhibit different strain-rate sensitivities.

Measurements for alloy AZ31 show that basal slip and twinning modes are approximately independent of strain-rate across a broad range of temperatures with strain-rate sensitivity coefficients of $m^{\alpha=1} = 1 \times 10^{-6}$ for the basal slip mode and $m^{\beta} = 1 \times 10^{-6}$ for the twinning modes (Korla and Chokshi, 2010; Watanabe and Ishikawa, 2009). In contrast, the strain-rate sensitivity coefficients for the prismatic and pyramidal slip modes were estimated to be $m^{\alpha=2} = 2.35 \times 10^{-2}$ and $m^{\alpha=3} = 7.42 \times 10^{-3}$, respectively (Ulacia et al., 2010; Watanabe and Ishikawa, 2009). Despite the fact that these individual values per mode are established, a single coefficient of strain-rate sensitivity for all modes is commonly used in modeling the strain-rate dependent behaviors of Mg alloys using crystal plasticity. Therefore, current models disregard the distinction of strain-rate sensitivity among different deformation mechanisms. The model in the work of (Wang et al., 2018) utilized a variable strain-rate sensitivity over deformation modes and successfully predicted strain-rate sensitive response of AZ31 over a range of imposed strain-rates; however, the experimentally measured values per deformation mode were still not numerically achieved, limiting the range of imposed strain-rates that the model captured. The development of crystal plasticity models that work for a wide range of imposed strain-rates is very challenging for metals and alloys such as Mg, which have several deformation modes. Low values of strain-rate sensitivity coefficient increase the stiffness of nonlinearity in the governing equations leading to computational failure (Knezevic et al., 2016b; Li et al., 2008).

In this paper, numerical robustness of the T-CPFE model is enhanced to consider measured values of strain-rate sensitivity per deformation mode. The developments here are motivated primarily from the fact that many metals exhibit low strain-rate sensitivity and often as function of deformation mode, the case with Mg alloys (Chapuis and Liu, 2019). The motivation also comes from an observation made in (Savage et al., 2017) that void growth-rates in voided cell computations introduce a strain-rate effect in the observed pressure dependence of the material. Such effects should be removed when studying the pressure dependence and comparing to analytical criterion. The significant role of the power law exponent in the extensional strain increase and subsequent development of localized deformation has been highlighted in (Peirce et al., 1983). The work varied m from a value of 0–0.005 for face-centered cubic (FCC) crystals under tension.

We seek to implement a robust numerical scheme in the T-CPFE model to eliminate the artificial scaling effect on stress with imposed strain-rate. The implementation relies on the visco-plastic power-law flow-rule, which relates the shearing-rate of a deformation system to the stress resolved on the system plane and in the glide direction (Hutchinson, 1976). The exponent n of the power-law relationship is the deformation system-level equivalent of the inverse of the strain-rate sensitivity coefficient m, which represents the dependence of the activation stress on strain-rate for fixed τ_c^s. The strain-rate sensitivity of material response m is $1/n$ with n defined as the slope of the ln-ln flow stress-strain-rate curve (Follansbee and Kocks, 1988; Hosford, 2010), $n = \frac{\partial \ln \dot{\varepsilon}}{\partial \ln \sigma}\Big|_{\varepsilon}$. The value of n is a deformation mechanism property, which can be measured experimentally from flow stress curves recorded at different strain-rates for a static i.e. fixed/constant microstructural state. Note that if microstructure evolves then the strain-rate sensitive flow stress is a consequence of a combination of the exponent, n, and evolving $\tau_c^s(\dot{\varepsilon})$.

Grains deforming plastically accommodate strain using a subset of available slip/twin systems. As multiple slip and twinning systems are involved, a sound criterion for activating these systems must be adopted. Criteria for identifying active systems prior to determining their shearing rate differ between rate-independent and rate dependent theories. Limitations of rate-independent formulations and advantages of rate dependent theory in terms of relating material rate dependence and unique determination of active slip systems have been discussed in (Peirce et al., 1983). Solutions to the selection of slip systems, the long-standing problem of the rate-independent theory of crystal elasto-plasticity, to produce an arbitrary deformation increment are presented in (Anand and Kothari, 1996; McGinty and McDowell, 2006; Zecevic and Knezevic, 2018). The selection can be achieved uniquely through the visco-plastic power-law formulism, which introduces strain-rate sensitivity into the deformation physics. In addition to representing the inverse of strain-rate sensitivity, sufficiently high value of the visco-plastic power-law exponent n ensures uniqueness in the solution to active slip/twin systems accommodating imposed strains. The distribution of shearing among the systems is collectively referred to as slip/twin activity. Predicting such activity is fundamental to predicting the flow strength and reorientations of the crystals. Due to numerical issues, the exponent n used e.g. in visco-plastic SC model is typically 20, which corresponds to $m = 0.05$. The value of $n = 20$ ensures uniqueness in selected deformation systems but much higher values than $n = 20$ are needed to accurately model the actual material strain-rate sensitivity at a constant resistance to slip/twin τ_c^s i.e. constant/static microstructure.

It is important to recognize that the strain-rate sensitivity embedded in the exponent for constant τ_c^s in conjunction with the strain-rate sensitive evolution of slip resistances, τ_c^s, describe strain-rate sensitive material behavior. The later contribution is described by the thermodynamic theory of slip, which states that dislocation glide is thermally activated in the strain-rate ranging approximately from 10^{-5} s^{-1} to 10^{5} s^{-1} (Kocks et al., 1975; Mecking and Kocks, 1981). Such strain-rate sensitive dislocation glide occurring in every plastically deforming grain in a polycrystal causes the macroscopic flow stress of the polycrystal to depend on strain-rate and temperature (Follansbee, 1986). Crystal plasticity modeling aims to relate the strain-rate sensitive glide of dislocations to the deformation of a grain or set of grains as well as to represent the constant structure strain-rate sensitivity under an imposed strain-rate and temperature conditions. Low values of n like 20–100 introduce an inaccurate decoupling between the strain-rate sensitive response of constant structure and strain-rate sensitive evolution of τ_c^s i.e. structure evolution. These issues are widely recognized (Kok et al., 2002; Peirce et al., 1983; Wang et al., 2018; Zecevic et al., 2016a) and this work offers a viable solution within T-CPFE.

In this article, a computationally efficient numerical procedure allowing for any value of the exponent governing material strain-rate sensitivity m is introduced into T-CPFE following the work involving a SC model presented in (Knezevic et al., 2016b) on polycrystalline Cu, which deforms by a single slip mode. The numerical method is termed the k-modification (k-mod) method. Until this original work, the use of these measured values of strain-rate sensitivity coefficients in crystal plasticity models was limited by numerical tractability i.e. the models were not able to take these measured values of strain-rate sensitivity per deformation mechanism. Taking advantage of these numerical improvements and advances made in the present work, measured values of strain-rate sensitivity per deformation mechanisms are employed in T-CPFE to investigate the strain-rate dependent behaviors of alloy AZ31 at room temperature. It is shown that the strain-rate dependent behavior of the alloy from 10^{-3} s^{-1} to 10^{3} s^{-1} can be accurately described by an accurate representation of strain-rate sensitivity associated with operative deformation mechanisms. The model accurately predicts flow stress and microstructure evolution for a broad range of strain-rates as a result of not only differing relative amounts of slip and twinning activity driven by a set of accurately characterized hardening law parameters but also deformation mechanism-level strain-rate sensitivities. Accordingly, the evolution of texture, anisotropy, asymmetry, and hardening behavior can be modeled across a wide range of applied strain-rates.

2. Modeling framework

The numerical scheme of the finite deformation crystal plasticity finite element (CPFE) model originally presented in (Kalidindi et al., 1992) is briefly summarized. In particular, the salient parts are outlined so that the proposed extension of CPFE and its implications to the numerical procedure have context. With this goal in mind, the kinematics and constitutive choices are focused on, while dislocation density-based hardening for slip and twinning (Ardeljan et al., 2016) is provided in appendix A. The particular version extended here is the T-CPFE (Ardeljan et al., 2016), which is a multi-level model linking the macro FE level at the highest scale and the Taylor-type polycrystalline model constitutive response at an integration point wherein the lowest level response of individual grains driven by slip/twinning is homogenized. The T-CPFE is implemented in finite element software ABAQUS as a user material subroutine (UMAT). The implicit finite element solver iteratively provides a best guess at time, τ $(t+\Delta t)$, of the deformation gradient, $\mathbf{F}$, for each gauss integration point in the finite elements based on the boundary conditions of the FE model. A set of state variables for each grain such as dislocation density for slip systems and twin volume fraction for each twin variant per grain is available from the previous increment, t. The UMAT updates the state variables, returns the volume average Cauchy stress, $\overline{\boldsymbol{\sigma}}$, and returns the Jacobian (i.e. the mapping between change in Cauchy stress components with respect to each component of the logarithmic strain) at the integration point. If the principles of virtual work are satisfied (boundary conditions and stress equilibrium), the solver moves on to the next time increment, otherwise the state variables are reset to the last converged state, and the updated Jacobian is used to create a new guess for the deformation gradient. Note that the Jacobian changes rate of convergence and whether convergence is achieved, but does not affect the solution. The following notation is utilized: tensor quantities are bold; tensor components and scalars are italic and not bold; indices s, α, t, and β denote slip systems, slip modes, twin systems, and twin modes, respectively; $\cdot$ is a dot product; and $\otimes$ is a tensor product.

2.1. Overview of CPFE

Since each FE integration point may be a polycrystal due either to twinning or including multiple grains (i.e. a Taylor polycrystalline aggregate), the Cauchy stress is taken as a volume average of crystal stresses at the integration point

$$\overline{\boldsymbol{\sigma}} = \langle \boldsymbol{\sigma} \rangle = \sum_{k=1}^{N_{grains}} v_k \boldsymbol{\sigma}_k, \tag{1}$$

where the sum of grain volume weights, v, is unity and $\langle\rangle$ denote the volume average.

The weighted grains embedded at an FE integration point undergo the same applied deformation gradient, $\mathbf{F}$, which is the intrinsic assumption of the Taylor model. The multiplicative decomposition of $\mathbf{F}$ leads to its plastic and elastic portions as

$$\mathbf{F} = \mathbf{F}^e \mathbf{F}^p. \tag{2}$$

In this decomposition, the intermediate configuration is plastically deformed by $\mathbf{F}^p$ and is stress-free meaning that the crystal lattice remains aligned with that in the undeformed configuration. The lattice stretch and rotation is accounted by $\mathbf{F}^e$. The rate of change of $\mathbf{F}^p$ is

$$\dot{\mathbf{F}}^p = \mathbf{L}^p \mathbf{F}^p, \tag{3}$$

which after the integration from the time at the beginning of the strain increment, t, to the end of the increment, $\tau = t+\Delta t$, is

$$\mathbf{F}^p(\tau) = exp(\mathbf{L}^p(\tau)\Delta t)\mathbf{F}^p(t). \tag{4}$$

The grain stress-strain relationship is

$$\mathbf{T} = \mathbf{C}\mathbf{E}^e, \text{ with } \mathbf{T} = \mathbf{F}^{e^{-1}} \boldsymbol{\tau} \mathbf{F}^{e^{-T}} = \mathbf{F}^{e^{-1}} \{(det\mathbf{F}^e)\boldsymbol{\sigma}\} \mathbf{F}^{e^{-T}} \text{ and } \mathbf{E}^e = \frac{1}{2}\left\{\mathbf{F}^{e^T}\mathbf{F}^e - \mathbf{I}\right\}, \tag{5}$$

where, $\mathbf{C}$ is the fourth-order elasticity tensor, $\mathbf{T}$ is the second Piola-Kirchhoff stress, which is the pull-back from current configuration of the contravariant Kirchoff stress $\boldsymbol{\tau}$ (also known as the weight Cauchy stress), and $\mathbf{E}^e$ is the Lagrangian strain. The elasticity stiffness tensor per grain is calculated based on the single-crystal elastic constants for Mg: $C_{11} = 59{,}500$ MPa, $C_{12} = 26{,}100$ MPa, $C_{13} = 21{,}800$ MPa, $C_{33} = 65{,}600$ MPa, $C_{44} = 16{,}300$ MPa (Duvvuru et al., 2007; Knezevic and Kalidindi, 2007; Landry and Knezevic, 2015; Slutsky and Garland, 1957). In order to calculate the stress, $\mathbf{F}^e$ must be known from $\mathbf{F}^e(\tau) = \mathbf{F}\mathbf{F}^{p^{-1}}(\tau) = \mathbf{F}\mathbf{F}^{p^{-1}}(t)\{\mathbf{I} - \Delta t\mathbf{L}^p(\tau)\}$. In order to evaluate $\mathbf{L}^p$, the applied velocity gradient tensor, $\mathbf{L}$, corresponding to $\mathbf{F}$, is additively decomposed to its elastic part, $\mathbf{L}^e$, and plastic part, $\mathbf{L}^p$. The plastic part accounts for plasticity due to slip and twinning. These kinematics equations are

$$\mathbf{L} = \mathbf{L}^e + \mathbf{L}^p = \mathbf{L}^e + \mathbf{L}^{sl} + \mathbf{L}^{tw} = \mathbf{L}^e + \sum_{s}^{N^{sl}} \dot{\gamma}^s \mathbf{S}_0^s + \sum_{t}^{N^{tw}} \dot{f}^t S^t \mathbf{S}_0^t, \tag{6}$$

where $\mathbf{S}_0^s = \mathbf{b}_0^s \otimes \mathbf{n}_0^s$ and $\mathbf{S}_0^t = \mathbf{b}_0^t \otimes \mathbf{n}_0^t$ are reference Schmid tensors for slip and twinning systems s and t, respectively, $\dot{\gamma}^s$ is the rate of shearing, S^t is the twin system shear strain, and $\dot{f}^t = \frac{\dot{\gamma}^t}{S^t}$ is the rate of twin volume fraction evolution, which is the pseudo-slip model (Kalidindi, 1998; Van Houtte, 1978). The Schmid tensors are based on the geometry of slip/twin system vectors, $\mathbf{b}_0^s$ and $\mathbf{b}_0^t$ are Burgers vectors and $\mathbf{n}_0^s$, and $\mathbf{n}_0^t$ are plane normal vectors. These vectors are time independent i.e. are in the reference configuration, 0. N^{sl} and N^{tw} are total number of slip and twin systems.

The standard power-law relationship of crystal visco-plasticity can be used to calculate the shear strain-rates for slip and twinning, $\dot{\gamma}^s$ and $\dot{\gamma}^t$, (Asaro and Needleman, 1985; Hutchinson, 1976; Kalidindi, 1998). Since the equation is equivalent for slip and twinning (except twinning is directional i.e. restricted to carry out positive shearing), for slip systems s, it is

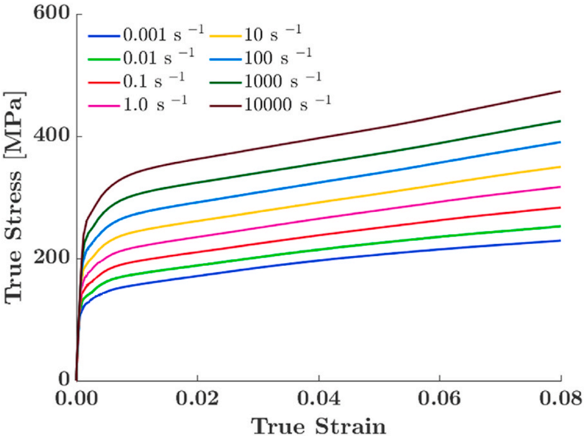

Fig. 1. Effect of the power-law exponent of $n = 20$ on the alloy AZ31 response in simple tension as a function of imposed strain-rate as indicated in the legend. The same value of n is used for every slip mode α and twin mode β.

$$\dot{\gamma}^s = \dot{\gamma}_0 \left(\frac{|\tau^s|}{\tau_c^s(\dot{\varepsilon}, T)} \right)^{\frac{1}{m}} sign(\tau^s), \tag{7}$$

where the resolved shear stress is calculated using $\tau^s = \mathbf{T} \cdot \mathbf{S}_0^s$, τ_c^s is the slip systems resistance, $\dot{\gamma}_0$ is the reference shearing rate used to scale the applied strain-rate ($\dot{\gamma}_0 = 0.001\ \mathrm{s}^{-1}$), and m is the strain-rate sensitivity. The power-law exponent, $\frac{1}{m} = n$, must be sufficiently high to ensure proper selection of slip/twin systems and, at the same time, should not introduce any extraneous *constant structure* (i.e. constant τ_c^s) strain-rate sensitivity. The latter is recognized as a significant issue when attempting to simulate high strain-rate deformation using crystal visco-plasticity models (Knezevic et al., 2016b; Zecevic et al., 2016a). The strain-rate sensitivity introduced by the power-law relation reduces as n increases. The strain-rate sensitivity embedded in the exponent should not be confused with the strain-rate sensitive evolution of slip resistances, τ_c^s, as described by the thermodynamics of slip (Follansbee and Kocks, 1988; Kocks et al., 1975). The evolution of slip/twin resistances, τ_c^s, originates from the *evolving structure*. The aim of the present work is both to relate the strain-rate sensitive glide of dislocations to the deformation of a grain or set of grains (see the hardening law in appendix A) and to represent the constant structure strain-rate sensitivity under an imposed strain-rate, as detail below.

2.2. Computationally efficient representation of strain-rate sensitivity per slip/twin mode using the k-modification (k-mod) method

The power-law visco-plasticity theory has proven effective in determining the single crystal yield surfaces of materials with many potential slip/twin systems. However, the power exponent also controls the strain-rate sensitivity of the response such that for $n \to \infty$, the shear-rates and stress become rate insensitive; however, increasing n above 100 is not computationally attractive since the simultaneous equations in $\boldsymbol{T}$ and τ_c^s becomes too stiff to solve numerically or take a prohibitive number of iterations (Knezevic et al., 2016b). Conversely, if n is too small ($n < 20$), the selection of active slip systems is affected.

The symmetric part of $\mathbf{L}^p$ is the plastic rate of stretching tensor

$$\mathbf{D}^p = \frac{1}{2} \left(\mathbf{L}^p + \mathbf{L}^{p^T} \right), \tag{8}$$

which is deviatoric, and an equivalent strain-rate to it is $\dot{\varepsilon} = \sqrt{\frac{2}{3} \mathbf{D}^p \cdot \mathbf{D}^p}$. The same rate of stretching is applied to every crystal, c, in a Taylor polycrystal, i.e.

$$\mathbf{D} = \langle \mathbf{D}^c \rangle = \mathbf{D}^c, \tag{9}$$

with

$$\mathbf{D}^{p,c} = \sum_s \dot{\gamma}^{s,c} \mathbf{P}_0^{s,c}, \tag{10}$$

where $\mathbf{P}_0^{s,c} = \frac{1}{2}(\mathbf{S}_0^{s,c} + (\mathbf{S}_0^{s,c})^T)$ is the symmetric part of the Schmid tensor for crystal c. The superscript c will be omitted from writing in the crystal equations that follow. In case the applied rate of stretching is scaled by $\lambda \neq 1$, Eq. (10) and Eq. (7) lead to

$$\lambda \mathbf{D}^p = \lambda \dot{\gamma}_0 \sum_s \mathbf{P}^s \left(\frac{|\mathbf{T} \cdot \mathbf{P}_0^s|}{\tau_c{}^s} \right)^n \mathrm{sgn}\left(\mathbf{T} \cdot \mathbf{P}_0^s \right) = \dot{\gamma}_0 \sum_s \mathbf{P}^s \left(\frac{|\lambda^{\frac{1}{n}} \mathbf{T} \cdot \mathbf{P}_0^s|}{\tau_c{}^s} \right)^n \mathrm{sgn}\left(\lambda^{\frac{1}{n}} \mathbf{T} \cdot \mathbf{P}_0^s \right). \tag{11}$$

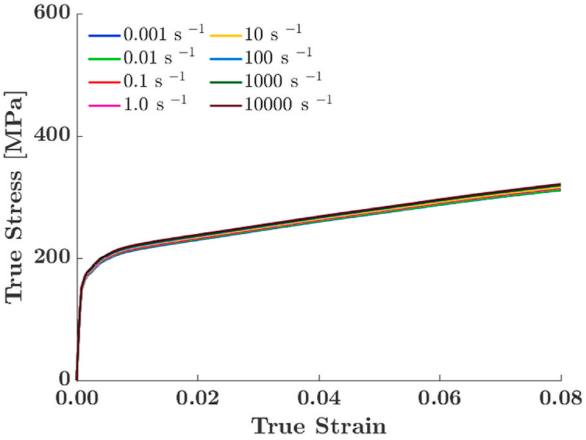

Fig. 2. Effect of the power-law exponent of $n = 20$ and $k = 19$ on the alloy response in simple tension as a function of imposed strain-rate as indicated in the legend. The k-mod formulation of $n(k+1) = 400$ approximately achieves a strain-rate insensitive response, which corresponds to the imposed strain-rate of 1.0. The same values of n and k are used for every deformation mode, α and β.

For constant τ_c^s, the equation on the right governs a strain-rate sensitive response that scales inversely with n. Evidently, the stress is scaled as $\lambda^{\frac{1}{n}}\mathbf{T}$, and raising n has the effect of removing the strain-rate sensitivity, i.e. $\lim_{n\to\infty}\lambda^{\frac{1}{n}} = 1$. Fig. 1 shows the effect of the power-law exponent of $n = 20$ (strain-rate sensitivity of $m = 0.05$) on stress-strain response of the alloy AZ31 in simple tension as a function of imposed strain-rate, $\dot{\varepsilon}$ (i.e. the scaling of the applied rate of stretching like $\lambda\mathbf{D}^p$). The reference shearing rate was constant, $\dot{\gamma}_0 = 0.001\ \mathrm{s}^{-1}$. The same value of n is used for every deformation mode, α and β. As is evident, the standard power-law equation of the visco-plasticity theory requires a correction to remove the superfluous strain-rate sensitivity that is introduced with inaccurately low values of n (i.e. high values of m).

The complexity for finding the solution of crystal stress given an imposed deformation scales with increasing value of the power-law exponent n. The value of n representative for strain-rate sensitive behavior of many metals is difficult to achieve numerically. Commonly used Newton-Raphson (NR) solution procedures converge for n in the range up to $n = 50$. Modified NR solution procedures are required to reach to about $n = 100$. As mentioned, for most metallic materials, such as stainless steel and Cu, the value of n needs to be significantly greater in order to capture their strain-rate sensitive response (Chen and Gray, 1996; Follansbee and Kocks, 1988; Hosford, 2010; Jahedi et al., 2015b; Knezevic et al., 2013a, 2016b). Modified NR procedures often encounter convergence problems for $n > 100$. As a result of $n > 100$, the non-linear equations turn out to be extremely stiff and prohibitively challenging to solve for stress. A way to achieve values of n representative of the strain-rate sensitivity of actual metallic materials numerically is adding an additional solution procedure loop to incrementally increase n. To this end, an obtained solution for a given n is used as a guess to calculate the next solution corresponding to a higher n. Such a solution procedure is computationally prohibitive and unpractical.

Another approach consists of eliminating the strain-rate sensitive response by embedding the norm of an applied rate of stretching, $|\mathbf{D}^p|$, into the reference shear rate, $\dot{\gamma}_0$. The approach makes the model strain-rate insensitive. A change in the magnitude but not sense of the applied rate of stretching, $\lambda\mathbf{D}^p$, will not change stress provided that τ_c^s is constant with strain-rate because $\dot{\gamma}_0 = |\lambda\mathbf{D}^p|$. The typical value of n used in this approach is $n = 20$, which ensures the proper selection of slip/twin systems and is efficient. The approach was used in many prior studies (Feather et al., 2019; Knezevic et al., 2013d; Kok et al., 2002). However, in addition to not capturing strain-rate sensitive response of materials, this approach has another major issue when attempting to implement it into FEM (Knezevic et al., 2013b; Knezevic et al., 2013c; Segurado et al., 2012; Zecevic et al., 2016a; Zecevic et al., 2015a, b). Since the stress is no longer a function of $|\mathbf{D}^p|$ but a function of four components of the normalized rate of stretching $\frac{\mathbf{D}^p}{|\mathbf{D}^p|}$, the solution for stress has dependent components. The Cauchy stress required by Abaqus will only have five (not six) independent components.

A solution to this problem allowing any value for the strain-rate sensitivity while being computationally efficient is a so-called the k-mod method (Knezevic et al., 2016b), which is summarized in the remainder of this section. The method is implemented in the T-CPFE model per deformation mode to model the strain-rate sensitive behavior of alloy AZ31.

The key component of the k-mod method is an appropriate modification of the applied rate of stretching at every FE integration point before evaluating the constitutive function for stress at the grain level. Specifically in place of any applied rate of plastic stretching denoted now by $\mathbf{D}^{p,app}$, we use a modified rate of stretching, $\mathbf{D}^p$, to solve for stress

$$\mathbf{D}^p = \frac{\mathbf{D}^{p,app}}{|\mathbf{D}^{p,app}|}|\mathbf{D}^{p,app}|^{\frac{1}{k+1}}. \tag{12}$$

As k increases, the norm of $\mathbf{D}^p$ approaches unity. The inverse relationship is $\mathbf{D}^{p,app} = \mathbf{D}^p|\mathbf{D}^{p,app}|^{\frac{k}{k+1}} = \mathbf{D}^p|\mathbf{D}^p|^k$. Thus, the norm of $\mathbf{D}^p$ is the $(k+1)^{\text{th}}$ root of $\mathbf{D}^{p,app}$. Note that powers and norms do not apply to the units but only to the values. Because $\mathbf{D}^e$ is small for a plasticized grain, whether we modify the plastic $\mathbf{D}^{p,app}$ or the total $\mathbf{D}^{app}$ in Eq. (12), results are not appreciably different. Since evaluating $\mathbf{D}^{p,app}$ requires an additional loop for the implicit integration, we elect to use $\mathbf{D}^{app}$ in order to avoid the computational cost associated with the third loop. The rate of deformation tensor $\mathbf{D}^{app}$ is provided as an Abaqus UMAT variable. As a result, the k-mod method introduces the following scaling to the stress while governing the amount of strain-rate sensitivity

$$\frac{\lambda\mathbf{D}^{app}}{|\lambda\mathbf{D}^{app}|}|\lambda\mathbf{D}^{app}|^{\frac{1}{k+1}} \approx \lambda^{\frac{1}{k+1}}\mathbf{D}^{p} = \dot{\gamma}_0\sum_{s}\mathbf{P}_0^s\left(\frac{\left|\lambda^{\frac{1}{(k+1)n}}\mathbf{T}\cdot\ \mathbf{P}_0^s\right|}{{\tau_c}^s}\right)^n \operatorname{sgn}\left(\lambda^{\frac{1}{(k+1)n}}\mathbf{T}\cdot\ \mathbf{P}_0^s\right). \tag{13}$$

The equation states that if the applied rate of stretching is arbitrarily altered to $\lambda\mathbf{D}^{app}$, the k-mod method modifies the rate of stretching from $\mathbf{D}^p$ to $\lambda^{\frac{1}{k+1}}\mathbf{D}^p$. As a consequence, the grain stresses, $\mathbf{T}$ i.e. $\boldsymbol{\sigma}$ scales according to $\lambda^{\frac{1}{(k+1)n}}\boldsymbol{\sigma}$ and, as a result, the homogenized macroscopic stress scales according to$\lambda^{\frac{1}{(k+1)n}}\overline{\boldsymbol{\sigma}}$. Note that, the scaling in Eqs. (11) and (13) has the same form, but in the former case the scaling is only by n ($\lambda^{\frac{1}{n}}\mathbf{T}$), while in the latter case by a combination of n and k ($\lambda^{\frac{1}{(k+1)n}}\mathbf{T}$). It should also be noted that the increase in k affects the scaling of the stretching and stress tensors but does not affect the relative contribution of active slip/twin systems. Selection of slip/twin systems and the strain-rate direction are defined only by n.

Grain stress solutions are different with n or with a combination of n and k as seen from Eqs. (11) and (13), respectively. To appreciate this scaling of the stress, consider the same scaling of the applied strain-rate (i.e. the rate of stretching $\lambda\mathbf{D}^p$) as in Fig. 1, while keeping the constant value for the reference shearing rate, $\dot{\gamma}_0 = 0.001\ \mathrm{s}^{-1}$. In the k-mod approach, any value of a strain-rate sensitivity as the material property can be realized by a combination of n and k. It is convenient to set $n = 20$ because it ensures proper selection of slip/twin systems and is computationally efficient, while only vary k. The scaling is demonstrated by rerunning the simulations from Fig. 1 after setting $k = 19$ and keeping $n = 20$ (i.e. $(k+1)n = 400$). The curves from Fig. 1 converge to a strain-rate sensitive response of $m = 0.0025$ in Fig. 2. The sensitivity of 0.0025 is typical for Cu (Follansbee, 1986) and many steels (Poulin et al., 2019). It should be noted that the exponent of 400 can also be achieved either by $n = 400$ and $k = 0$ or another combination of n and k like $n = 50$ and $k = 7$. These would produce the same results but would not be as efficient as the combination of $n = 20$ and $k = 19$ because the computational time to solve for the stress given the rate of stretching increases with n to 50 or to 400 but remains the same with increase in k. Changing the value of k does not influence the convergence of the NR solution for stress and, therefore, it does not influence the time to solving the power-law with a given value of n. Importantly, different combinations of n and k can be used per slip/twin mode governing their individual strain-rate sensitivities.

As the k-mod method alters the rate of plastic stretching accommodated by grains from $\mathbf{D}^{p,app}$ to $\mathbf{D}^p$, to ensure that the grains actually accommodate the applied rate of stretching, $\mathbf{D}^{p,app}$, the calculated shearing rates scale using

$$\mathbf{D}^{p,app} = \frac{|\mathbf{D}^{app}|}{|\mathbf{D}^{app}|^{\frac{1}{k+1}}}\sum_{s}\mathbf{P}_0^s\dot{\gamma}^s = \sum_{s}\mathbf{P}_0^s\dot{\gamma}_{k-\mathrm{mod}}^s, \tag{14}$$

such that the shearing rates are normalized in CPFE as

$$\dot{\gamma}_{k-\mathrm{mod}}^s = \frac{|\mathbf{D}^{app}|}{|\mathbf{D}^{app}|^{\frac{1}{k+1}}}\dot{\gamma}_0\left(\frac{\left|\mathbf{T}\cdot\ \mathbf{P}_0^s\right|}{{\tau_c}^s}\right)^n \operatorname{sgn}\left(\mathbf{T}\cdot\ \mathbf{P}_0^s\right). \tag{15}$$

Finally, as the Jacobian matrix plays a central role in the rate of convergence of the equilibrium governing equation in the FE framework (Bathe, 1996), a modification to the analytical CPFE Jacobian matrix due to the k-mod implementation is implemented. The overall Jacobian matrix is defined as a derivative of the Cauchy stress tensor with respect to the logarithmic strain tensor provided by ABAQUS. The matrix revises the deformation field at each FE integration point in order to iteratively satisfy the principle of virtual work using the Newton-type implicit FE iterations (Anand, 2004; Delannay et al., 2003). To accommodate the k-mod, the modification pertains to the relationship between $\dot{\gamma}_{k-\mathrm{mod}}^s$and $\mathbf{T}$, which is approximated as follows

$$\frac{\partial\Delta\gamma_{k-\mathrm{mod}}^s}{\partial\mathbf{T}} = |\mathbf{D}^{app}|^{\frac{k}{k+1}}\frac{\partial\Delta\gamma^s}{\partial\mathbf{T}}, \tag{16}$$

where $\frac{\partial\Delta\gamma^s}{\partial\mathbf{T}}$ is computed as in the original model. If the analytical form for the derivative $\frac{\partial\mathbf{D}^{p,app}}{\partial\mathbf{T}}$ is involved in Eq. (16), a computationally expensive matrix inversion operation would be involved. We have observed that setting $\frac{\partial\mathbf{D}^{app}}{\partial\mathbf{T}} = 0$ has no apparent impact on the convergence rate of the stress solution, even in applications with rapid fluctuations of applied strain-rates such as in Taylor cylinder impact simulations; therefore, the computational expense of the matrix inversion suggests a Jacobian modification beyond Eq. (16) is unwarranted. For completeness, Appendix B provides the full analytical Jacobian if $\mathbf{D}^{p,app}$ is considered instead of $\mathbf{D}^{app}$, beginning from Eq. (13).

In closing this section, we mention that while modifying the T-CPFE model for the inclusion of the k-mod method, we enabled the uses of threaded parallelization in the code, while still maintaining the option to uses MPI parallelization. Threaded parallelization is a shared memory parallelization method where all parallel workers or ‘threads’ have access to all the variables all of the time. As opposed to MPI parallelization where each parallel worker or ‘process’ has its own copy of all the variables that only it has access to. This does not have inherent performance improvements but in an application such as CPFE where there are several arrays that are of size (# elements, # integration points, # of crystals per integration) this reduces the number of duplicates of these potentially very large arrays which is required for each MPI process. To quantify the benefit of this change a 64 element model with 6 grains embedded at each integration point was run with each version of the code, with 16 CPUs each. The memory usage of this simulation was 6.68 GB for the old MPI only version of the model, and 0.70 GB for the threaded parallelization version. This is about a 90% decrease in memory

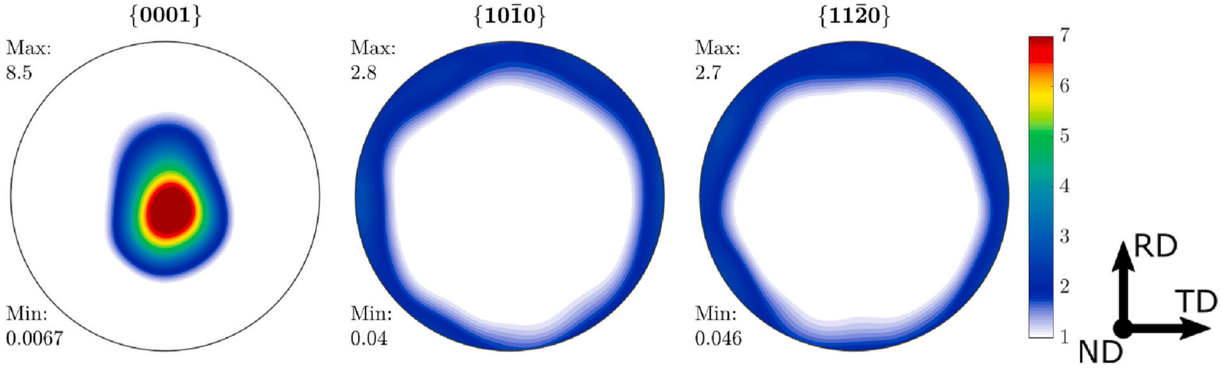

Fig. 3. Pole figures showing the initial measured texture of the alloy. Measured texture using electron backscattered diffraction (EBSD) over a large area is compacted to 3,072 crystal orientations for simulations. Pole figures of the initial texture used in the simulations are indistinguishable from the measured ones depicted in the figure and are not shown.

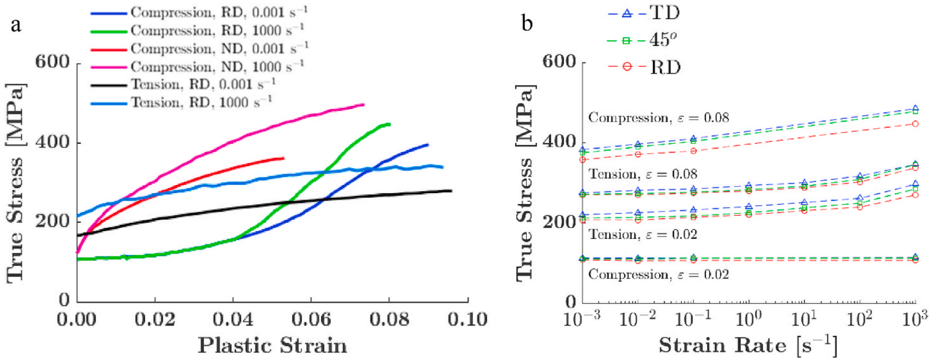

Fig. 4. (a) True stress-plastic strain response of annealed alloy AZ31B–O Mg sheet in compression and tension along the rolling direction (RD) and in compression along the normal direction (ND) at room temperature as a function of strain-rate. (b) True stress versus strain-rate (logarithmic scale) trend lines at two strain levels (0.02 and 0.08) for the sheet deformed in simple compression and tension along the three in-plane direction (RD, 45°, and TD). The symbols are measuring points. The data is taken from (Kurukuri et al., 2014).

requirements, enabling the use of larger element count models. A computer workstation of Intel(R) Xeon(R) Gold 6130 CPU @ 2.10 GHz with 32 physical cores and 772 GB RAM was used to perform the simulations in this work.

3. Experimental data

Experimental data utilized in the present work are taken from (Kurukuri et al., 2014) for a rolled sheet of alloy AZ31B (3.0% Al, 1.1% Zn, 0.49% Mn) in the annealed condition (O-temper) with equiaxed grains and a 12 µm average diameter. Pole figures showing the initial texture in the sheet are shown in Fig. 3. The sheet exhibits a typical, strong basal texture with the majority of grains in the sheet being oriented with their crystallographic **c**-axes along the sheet normal direction (ND). There is more spreading/tilting in the rolling direction (RD) compared to the transverse direction (TD). The sense of loading (tension, compression) and orientation of loading (RD, TD, ND) relative to the initial crystallographic texture govern the activity of deformation mechanisms accommodating the plasticity.

In the work of (Kurukuri et al., 2014), the alloy was tested under strain-rates ranging from 10^{-3} s^{-1} to 10^{3} s^{-1} at room temperature. To characterize the effect of sheet orientation and strain-rate on flow stress anisotropy and tension/compression asymmetry, the strain-rate sensitive flow stress was measured in tension along the RD, 45°, and TD and in compression along the RD, 45°, TD, and ND. Fig. 4a shows that the in-plane (RD) flow stress in compression is approximately strain-rate insensitive for the early portion of deformation. As the compressive deformation proceeds, the material starts to exhibit increasingly strain-rate sensitive behavior. The material is much stronger in compression along ND relative to the in-plane compressive loading. The ND compressive response exhibits some strain-rate sensitivity in terms of the initial yield strength. However, the rate of strain hardening increases for higher strain-rate loading. Under loading in tension, the alloy exhibits strong strain-rate sensitivity, which is approximately constant throughout the deformation. The alloy exhibits pronounced tension/compression asymmetry that increases with strain-rate.

The strain-rate sensitivity under tension and compression along three in-plane orientations (RD, 45°, and TD) is further illustrates in Fig. 4b, in which true stress vs. strain-rate from 10^{-3} s^{-1} to 10^{3} s^{-1} is plotted for the strain levels of 0.02 and 0.08. The figure first

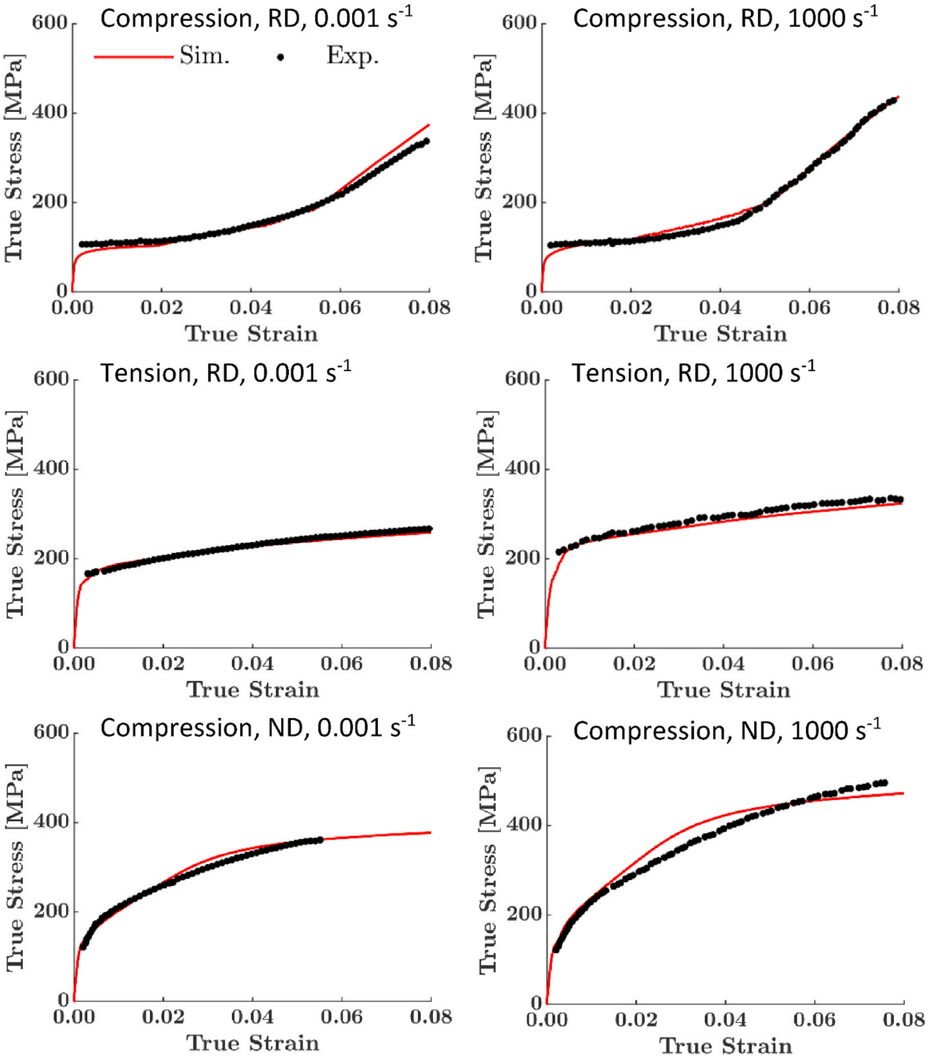

Fig. 5. Comparison of measured and simulated true stress–true strain responses of the alloy in compression and tension along the rolling direction (RD) and in compression along the normal direction (ND) at room temperature under two strain-rates. The simulations are based on the measured values of strain-rate sensitivity per deformation mode.

shows that the material exhibits mild in-plane anisotropy with the TD direction being the strongest. The RD is the least strong. Looking at the texture (Fig. 3), such behavior is expected since there is slightly more grains tilted with their **c**-axis towards RD than TD. The data further shows that there is a clear increase in strength with the strain-rate in all the three tested directions in tension. Interestingly, the trend lines for tension along the three directions show similar slope at both strain levels. The figure also reveals that the degree of tension/compression asymmetry increases with strain-rate, primarily at low strain levels. This is because the in-plane compressive response is approximately strain-rate insensitive at low strains (0.02). The low slope of the trend lines clearly indicates this. At higher strains (0.08), the compressive strain-rate sensitivity is strong. The trend lines indicate comparable or even higher slope than that in tension. Rapid hardening in compression makes the compressive strength exceed the tensile strength with plastic strain.

The complex behavior of the alloy with strain and strain-rate is attempted to be interpreted here using the enhanced T-CPFE model, which incorporates the true values of strain-rate sensitivity of individual deformation mechanisms that activate as a function of texture, loading sense. The measured values of strain-rate dependency of individual deformation mechanisms will be validated, while predicting the comprehensive mechanical data.

4. Results

Simulations were performed using a simple cubical cell consisted of 64 continuum three-dimensional eight-nodal (C3D8) elements. Simple tension/compression boundary conditions were prescribed by specifying displacements along the loading direction while ensuring the stress-free conditions on the lateral faces (Jahedi et al., 2015a). The imposed strain-rate in each simulation was consistent

Table 1a
Fitting parameters for the evolution of slip resistance per slip mode.

Parameter	Basal, $\alpha = 1$	Prismatic, $\alpha = 2$	Pyramidal, $\alpha = 3$
τ_0^α [MPa]	3.9	38	92
k_1^α [m^{-1}]	6E+6	1.8E+6	1.8E+8
g^α	1.4E-4	1.2E-4	6.2E-3
D^α [MPa]	100	150	225
q^α	130	250	720
H_1^α	0.007	0.014	0.13
H_2^α	0.1	0.20	3.53
H_3^α	0.1	0.20	2.12

Table 1b
Fitting parameters for the evolution of twin resistance per twin mode.

Parameter	Extension, $\beta = 1$	Contraction, $\beta = 2$
τ_{crit}^β [MPa]	15	90
τ_{prop}^β [MPa]	7	60
H_0^β[MPa]$\sqrt{\mathrm{m}}$	0.09	0.13
$C^{\alpha\beta}, \alpha = 1$	200	200
$C^{\alpha\beta}, \alpha = 2$	300	300
$C^{\alpha\beta}, \alpha = 3$	600	600

with the experiment and the only change from test to test is the strain-rate and prescribed loading direction. The initial texture was represented using 3,072 equally weighted crystal orientations to initialize the model. A Taylor sub-polycrystal consisted of 6 grains was embedded at each integration point via a random assignment. Every orientation is allowed to develop multiple twin variants and, therefore, the number of orientations at each integration point can increase with plastic strain very quickly. Four stress-strain curves were used in fitting of the model parameters for AZ31 while calculating the stress-strain response. Two remaining curves as well as the evolution of texture and twinning can be regarded as predictions.

In the simulations, basal **a** $\{0001\}\langle\bar{1}\bar{1}20\rangle$, prismatic **a** $\{\bar{1}100\}\langle\bar{1}\bar{1}20\rangle$, and pyramidal **c**+**a** $\{10\bar{1}1\}\langle\bar{1}\bar{1}23\rangle$ or type I and $\{\bar{1}\bar{1}22\}\langle\bar{1}\bar{1}2\bar{3}\rangle$ or type II slip modes and **c**-axis extension $\{10\bar{1}2\}\langle\bar{1}011\rangle$ (TTW) and **c**-axis contraction $\{10\bar{1}1\}\langle10\bar{1}\bar{2}\rangle$ (CTW) twin modes were made available. In addition, secondary twinning facilitating a common double twinning sequence $\{10\bar{1}1\}-\{10\bar{1}2\}$ (DTW) was allowed to operate. The TTW accommodates a shearing strain of 0.1289, while reorienting the crystal orientation of the twinned domain for about 86° about the $\langle11\bar{2}0\rangle$ direction. The CTW produces a shear of 0.1377, while reorienting the crystal orientation of the twinned domain for about 56° about the $\langle11\bar{2}0\rangle$ direction (Yoo, 1981). While the TTW are fast growing and thick (Al-Samman and Gottstein, 2008; Barnett, 2007a; Jahedi et al., 2017), the CTW are thin (Al-Samman and Gottstein, 2008; Barnett, 2007b; Knezevic et al., 2010). The morphology of the latter twins is due to the creation of a TTW within the primary CTW lamella hindering its growth. The hardening law parameters are adjusted so that the slip/twin resistances evolve to provide the appropriate ratios of active deformation modes for predictions of stress-strain, texture, and twinning.

Fig. 5 compares measured and simulated true stress–true strain responses for the alloy in compression and tension along the RD and in compression along the ND at room temperature under two strain-rates (10^{-3} s^{-1} and 10^3 s^{-1}). The figure illustrates that the model successfully captures the phenomena pertaining to the effect of increase in the strain-rate on mechanical response using a single set of hardening parameters (Table 1). The hardening parameters were adjusted for the selected T-CPFE homogenization scheme, the CG twinning model, and the selected hardening law to reproduce the experimental data. In order to capture the mechanical response over a broad range of strain-rates, the following parameters associated with the hardening law for slip and twinning are fit. The parameters for slip are: the initial slip resistance, τ_0^α, trapping rate coefficient, k_1^α, activation barrier for de-pinning, g^α, drag stress, D^α, rate co-efficient q^α, and Hall-Petch-like coefficients,H_i^α. The parameters for twinning are: the nucleation stress, τ_{crit}^β, propagation stress, τ_{prop}^β, interaction matrices, $C^{\beta\alpha}$, and Hall-Petch-like coefficients H_0^β. The fitting procedure starts with varying the initial resistances to fit yield stress. Next, k_1^α, is adjusted such that the initial hardening slope is reproduced. Next, g^α, D^α, interaction matrices, and Hall-Petch-like coefficients are adjusted to match the hardening behavior. Finally, q^α is adjusted to capture the later stage of the hardening behavior. The parameters are fit while monitoring deformation mechanism activities and the evolution of texture and twinning.

Despite the relaxed Taylor assumptions afforded by the T-CPFE model, the Talor-type homogenization over 6 single crystals and their twins can still suffer from over or under activation of deformation mechanisms due to the geometric constraint. This effect primarily results in the case of this AZ31 alloy in a lower basal slip resistance and larger ratio between basal and other between slip

Table 2a
Strain-rate sensitivity per slip mode, m^{α}, achieved in the model by a combination of n^{α} and k^{α}. These values are measured data from the literature: $m^{\alpha=1} = 1 \times 10^{-6}$ for basal slip, $m^{\alpha=2} = 2.35 \times 10^{-2}$ for prismatic slip, and $m^{\alpha=3} = 7.42 \times 10^{-3}$ for pyramidal slip (Korla and Chokshi, 2010; Ulacia et al., 2010; Watanabe and Ishikawa, 2009).

Parameter	Basal, $\alpha = 1$	Prismatic, $\alpha = 2$	Pyramidal, $\alpha = 3$
n^{α}	20	20	20
k^{α}	49999	1.28	5.74
$n^{\alpha}\ (k^{\alpha} + 1)$	1000000	42.6	134.8
m^{α}	0.000001	0.0235	0.00742

Table 2b
Strain-rate sensitivity per twin mode, m^{β}, achieved in the model by a combination of n^{β} and k^{β}. Twinning modes are considered independent on strain-rate with the strain-rate sensitivity coefficient of $m^{\beta} = 1 \times 10^{-6}$ (Korla and Chokshi, 2010; Watanabe and Ishikawa, 2009).

Parameter	Extension, $\beta = 1$	Contraction, $\beta = 2$
n^{β}	20	20
k^{β}	49999	49999
$n^{\beta}\ (k^{\beta} + 1)$	1000000	1000000
m^{β}	0.000001	0.000001

modes when compared to other homogenization methods which better approximate the matrix constraint (Barnett, 2003; Tomé, 1999). As a result, substantially varying the number of grains embedded at integration points may require slight readjustment of the parameters. The simulations are based on the measured values of strain-rate sensitivity per deformation mode (Table 2). In particular, approximately strain-rate independent response is predicted for the in-plane compression to strains less than ~0.04, whereas the increasing strain-rate sensitivity is predicted for strains greater than ~0.04. The higher strength in compression along ND relative to the in-plane compression and, in particular, the increase in the rate of strain hardening with strain-rate for the ND compression are predicted well. The strong and approximately constant strain-rate sensitivity with plastic strain is predicted well under loading in tension. As a consequence of the different strain-rate sensitivity exhibited by the material in tension vs compression, the pronounced tension/compression asymmetry increases with strain-rate, which is also predicted well by the model.

Fig. 6 shows the predicted relative activities of deformation mechanisms accommodating plastic deformation of the alloy under the deformation conditions corresponding to Fig. 5. The activity plots include the activity in the parent and the twinned domains. The model adjusts deformation mechanisms accommodating the plastic strain based on the evolution of slip/twin resistances in order to predict the deformation behavior of the alloy. The typical sigmoidal upwards shape of the curves recorded under compression in RD is indication of profuse twinning in the first stages of deformation. Deformation by profuse extension twinning is followed by rapid strain-hardening owing to the subsequent activation of non-basal slip systems. The origin of such hardening is in the crystal lattice reorientation in the twinned domains. The twinned domains are harder than the parent orientation with respect to the loading direction (Asgari et al., 1997; Knezevic and Beyerlein, 2018; Knezevic et al., 2012). Hard pyramidal slip systems activate in the twinned domains (Clausen et al., 2008; Jain and Agnew, 2007; Lentz et al., 2015; Lou et al., 2007; Proust et al., 2009b; Risse et al., 2017). It is worth noting that the strength does not tend to substantially increase at/after the onset of twinning but after the extension twinning fraction increases with the plastic strain. The shear strain of $S^{t} = 0.1289$ intrinsic to the extension twins corresponds to a maximum plastic strain of about 0.0744 (Ghorbanpour et al., 2020b; Knezevic et al., 2010). The value follows from a simple theoretical analysis of the plastic strain accommodated by twinning, which is expressed as $\mathbf{D}^{tw} = \sum_{t}^{N^{tw}} \dot{\gamma}^{t} \mathbf{P}_{0}^{t} = \sum_{t}^{N^{tw}} \dot{f}^{\beta} S^{t} \mathbf{P}_{0}^{t}$. The rate of change of the twin volume fraction per particular twin system($\dot{f}^{t}$)is proportional to the shear rate on the twin system ($\dot{\gamma}^{t}$) and inversely proportional to the characteristic shear strain $\dot{f}^{t} = \frac{\dot{\gamma}^{t}}{S^{t}}$. Upon the time integration, the relationship is $\Delta f^{t} = \frac{\Delta\gamma^{t}}{S^{t}}$. With further integration over n strain increments, the accumulated twin volume fraction of a particular twin system, t, can reach unity (i.e. $\sum_{1}^{n} \Delta f^{t} = 1$), which means that the particular twin system accommodated the maximum possible amount of shear strain (i.e. $S^{t} = \sum_{1}^{n} \Delta\gamma^{t}$). In this case, the whole volume of the given parent grain completely reoriented into the twin variant t. Therefore, physically it is not possible to have any other twin variant active in this particular grain. In contrast, if multiple twin variants activate in a given grain then none of them can rich a volume fraction of unity but only sum of their volumes can reach unity. The corresponding equivalent plastic strain $\sqrt{\frac{2}{3}\mathbf{D}^{tw} \cdot \mathbf{D}^{tw}} = 0.0744$. As a result, the activity of extension twinning starts saturating shortly after the corresponding amount of the compressive plastic strain. With the extension twinning increasing with the plastic strain, crystallographic slip deformation mechanism activate more to accommodate the continuously imposed strain. Secondary twinning can also activate. These twins re-orient texture from soft (basal slip) to hard (pyramidal slip) orientations.

In addition, twins subdivide parent grains giving rise to the barrier Hall-Petch-like hardening effect (Asgari et al., 1997; Bouvier

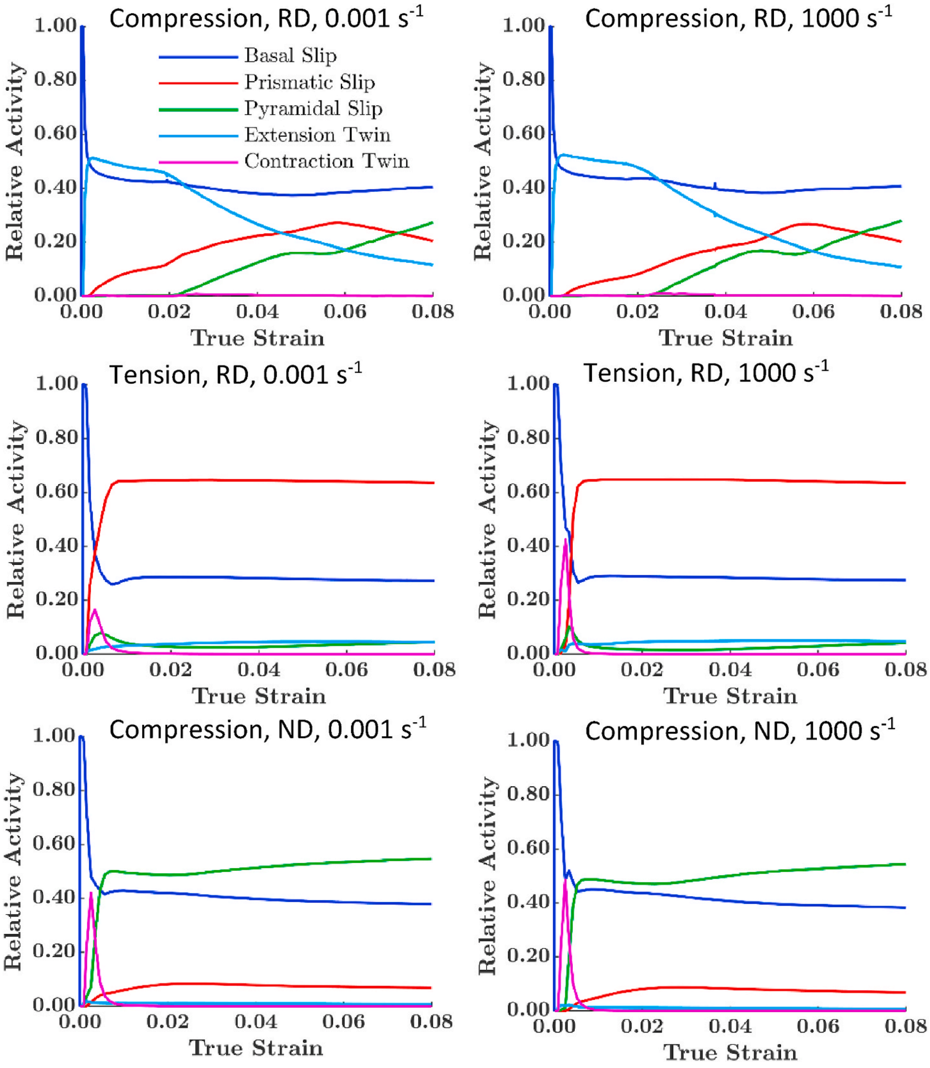

Fig. 6. Predicted activities of deformation mechanisms accommodating plastic deformation of the alloy in the deformation conditions indicated in the figure. The plots include activities in both the parent grains and the twinned domains.

et al., 2012; Kaschner et al., 2007; Proust et al., 2007; Savage et al., 2021b). The mechanism of barrier hardening is understood in terms of dislocations accumulating in the vicinity of the grain/twin interfaces. The alloy AZ31 is known to exhibit a variation in the Hall-Petch slope (Barnett et al., 2004; Yuan et al., 2011). This is an indication that the barrier effect should be associated with deformation systems, as is done in the present work. The values are fit for grains containing twins to reproduce the macroscopic true stress-true strain curves, while the grain size effect in embedded in the initial resistances. To this end, extension twins cause small barrier as reflected by small values of H_1^α because they grow quickly and dislocations can easily be transmitted (Molodov et al., 2017). As a result, the initial plateau in the stress-strain response arises. In contrast, contraction twins create a large barrier effect hardening (Knezevic et al., 2010), as reflected by large values of H_2^α. These contraction twins are very thin as they often develop extension twins, which is a commonly observed double twinning sequence (DTW). This trend of the CTW and DTW having higher barrier term values that the TTW is in agreement with experimental observations that the CTW/DTW effectively restrict the mean free path of pyramidal dislocations (Ardeljan et al., 2016; Knezevic et al., 2010). Some hardening due to twinning could arise from the so called Basinski-mechanism, which has to do with the transmutations of stored dislocations from the parent grain to the twinned domain (Basinski et al., 1997). However, this mechanism is small in Mg alloys since twins develop early in the deformation when the level of dislocation density in grains is low (El Kadiri and Oppedal, 2010; Knezevic et al., 2010). The in-plane tensile response is a consequence of prismatic slip primarily, while the ND compression response is a consequence of pyramidal and basal slip and contraction twinning. The decreasing hardening rates recorded in tension and ND compression indicate the slip dominated deformation. As already elaborated, the CTW causes significant barrier effect hardening to pyramidal slip.

TTW plays a significant role in texture evolution during in-plane compression. Fig. 7 and Fig. 8 show predicted twin volume

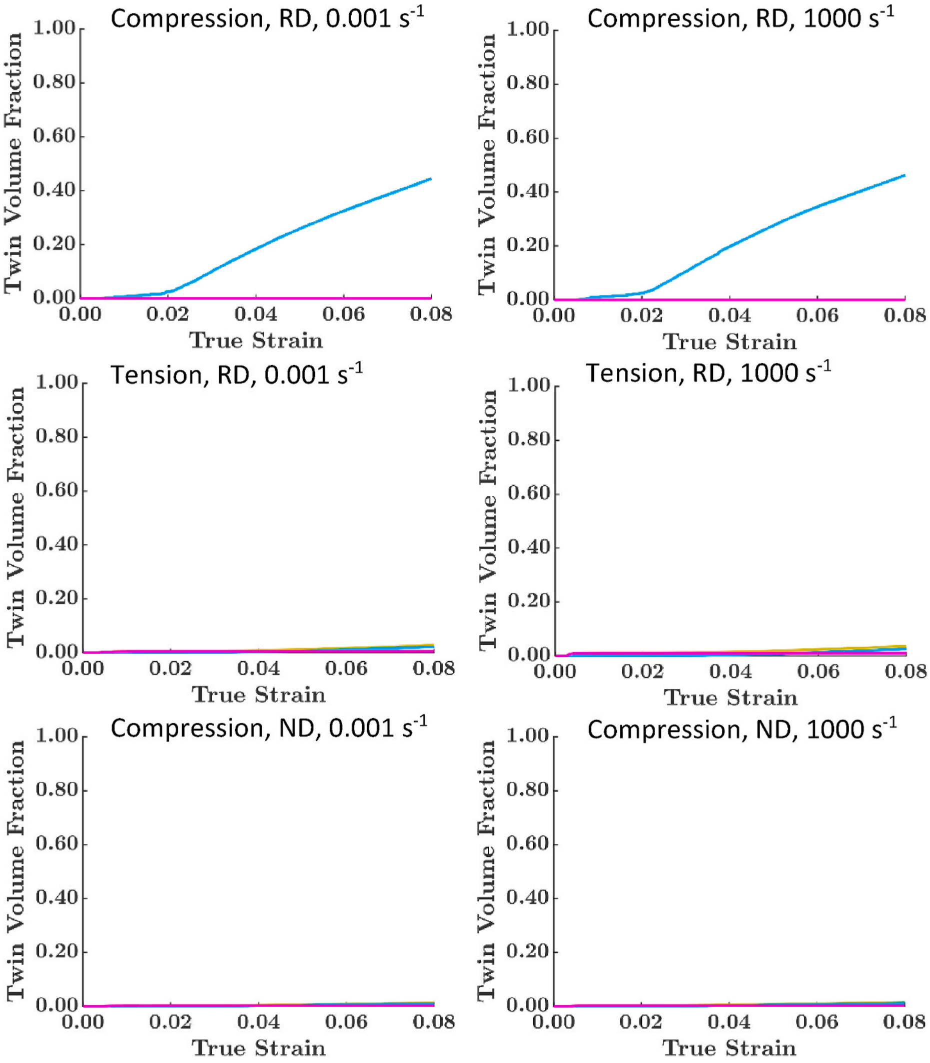

Fig. 7. Predicted twin volume fraction evolution during the deformation conditions indicated in the figure.

fractions and texture evolution, respectively. These results are consistent with many measurements from the literature like (Chun and Davies, 2011; Khan et al., 2011; Knezevic et al., 2010; Pandey et al., 2015; Paramatmuni and Kanjarla, 2019; Proust et al., 2009a). TTW and basal slip explain the texture formation in compression. The activity of prismatic and pyramidal slip increases with plastic strain to cooperate with the basal slip activity. These slip modes activate within extension twin domains and are responsible for hardening because the pyramidal slip is hard in particular. The cooperative action of prismatic and basal slip explain the texture formation in tension and pyramidal and basal slip explain the texture formation in ND compression. The activity of twinning in ND compression and in plane tension is small. In general, the activities at 10^{-3} s^{-1} and 10^{3} s^{-1} are similar but as such are the origin of the strain-rate sensitive deformation behavior of the alloy. The major difference is that there is a little more twinning at 10^{3} s^{-1} than at 10^{-3} s^{-1}. Because crystallographic slip is strain-rate sensitive and therefore more difficult under higher strain-rates, twinning as insensitive to strain-rate is promoted with strain-rate. Therefore, there is more hardening due to twinning under such deformation conditions. In particular, the higher hardening rates under high strain-rate deformation arise from the reduction of the slip length of mobile dislocations due to more activity of CTW/DTW. Qualitatively, the texture evolution is not a strong function of strain rate meaning that the shape change is accommodated by similar deformation mechanisms over a broad range of strain-rates. A number of studies have made similar observations for a range of materials (Ardeljan et al., 2016; Kabirian et al., 2015; Khan et al., 2011; Knezevic et al., 2013d, 2014; Pandey et al., 2015; Paramore et al., 2015). With the increased number of dislocation sources created at higher strain rates, the twin volume fractions slightly increase with the deformation rate (Song and Gray, 1995). Grains are often observed to contain slightly thinner lamellae under high strain rate deformation rather than fewer thicker lamellae developing under quasi-static deformation (Song and Gray, 1995b). Such microstructural evolution changes as a function of strain rate introduce only secondary effects on texture evolution and underlying activity of deformation mechanisms.

Fig. 9 shows predicted true stress versus strain-rate trend lines at two strain levels (0.02 and 0.08) superimposed over the trend lines

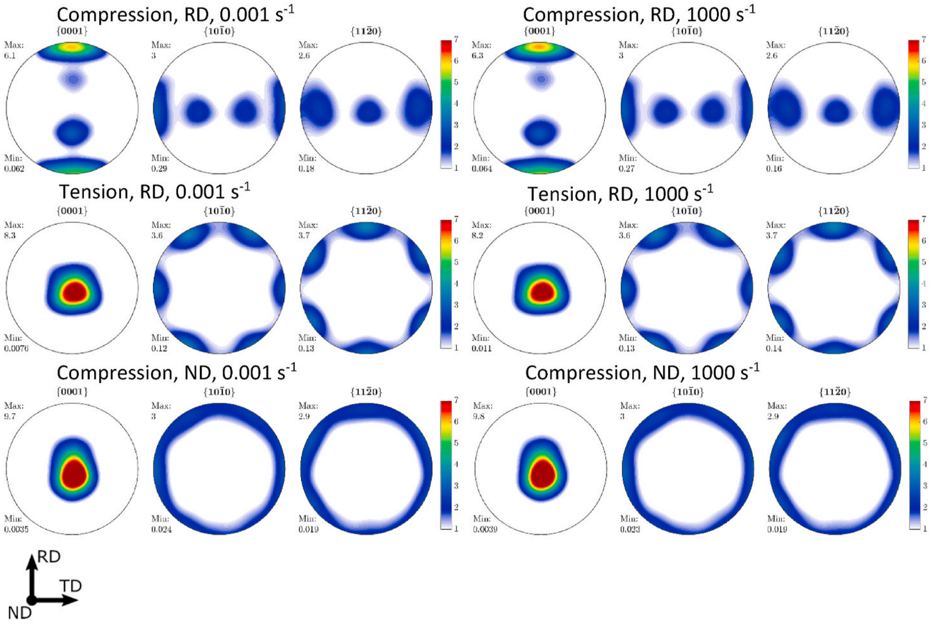

Fig. 8. Pole figures showing predicted texture in the alloy after deformation under the conditions indicated in the figure to a strain of 0.08.

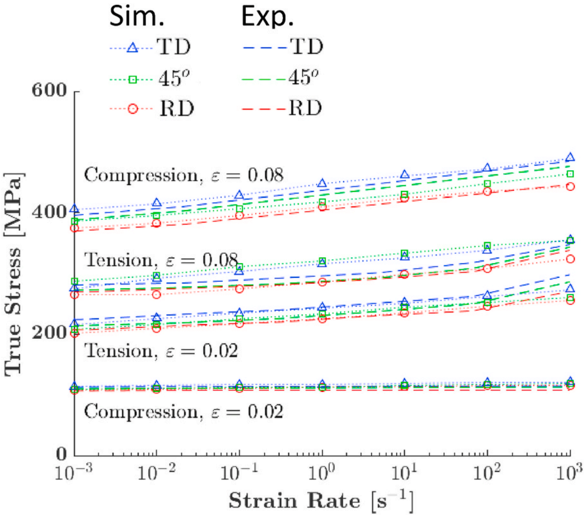

Fig. 9. Predicted true stress versus strain-rate trend lines at two strain levels (0.02 and 0.08) superimposed over the trend lines from Fig. 3b for the sheet deformed in simple compression and tension along the three in-plane direction (RD, 45°, and TD). The symbols are predicted points.

from Fig. 3b. The model successfully predicts the trend that TD is the strongest and RD is the weakest direction. Moreover, the model predicts that the in-plane compressive response is strain-rate insensitive (the low slope) at the lower strain level (0.02) for all three tested direction, since basal slip and extension twinning-dominated the plasticity. The model also predicts that the compressive strain-rate sensitivity increases at the higher strain level (0.08) due to the activation of pyramidal and prismatic slip systems. The model predicts the increase in strength with the strain-rate in all the three tested directions in tension. Such behavior is attributed to the strain-rate dependency of deformation mechanisms other than extension twinning and basal slip. Interestingly, the trend lines for tension along the three direction show similar slope at both strain levels. This is because there is no shift in deformation mechanisms during tensile deformation. Finally, it is not surprising that the model successfully predicts the increase in the degree of tension/compression asymmetry with increase in the strain-rate. These good predictions result from proper modeling of deformation mechanisms strain-rate sensitivity and the strain-rate sensitive evolution of slip/twin resistances.

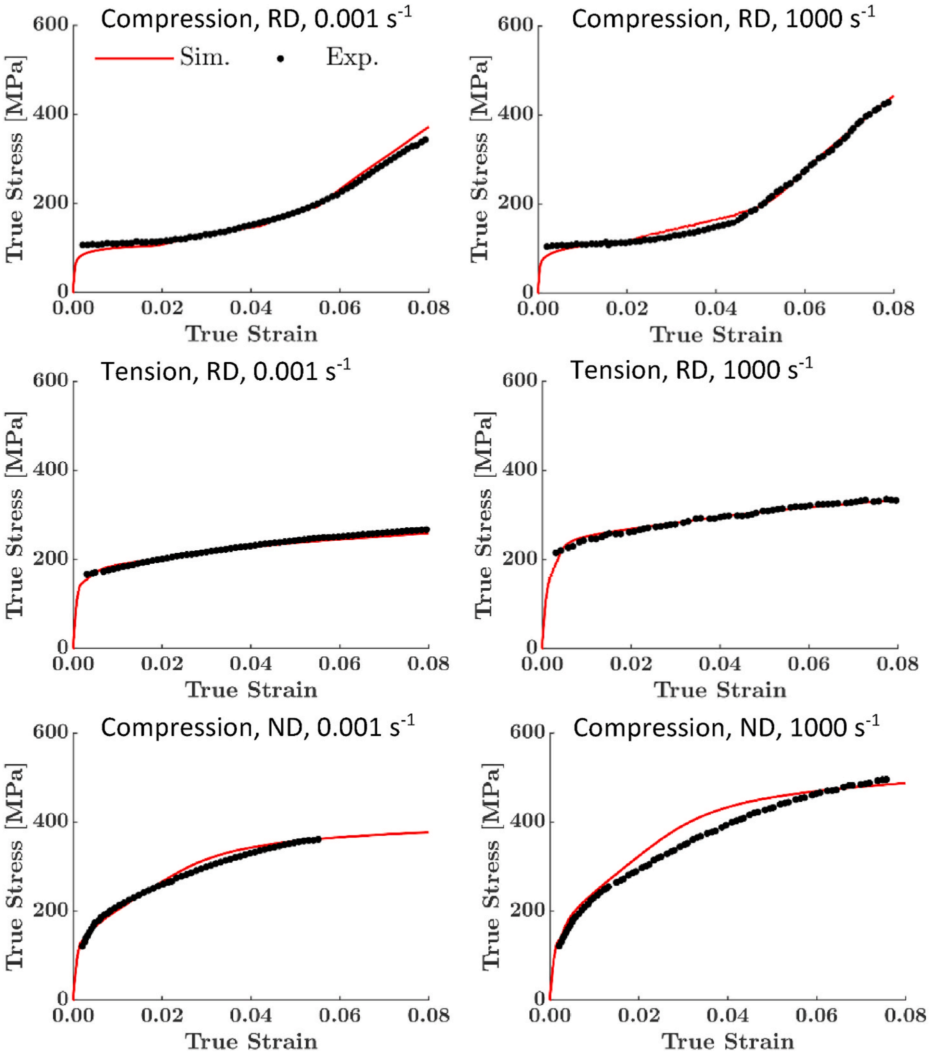

Fig. 10. Comparison of measured and simulated true stress–true strain responses for the alloy corresponding to Fig. 5 with simulations performed using adjusted values of strain-rate sensitivity per deformation mode.

5. Discussions

Strain-rate sensitivity is an essential material property governing the strain-rate dependent flow stress response and formability as a function of imposed strain-rate. Understanding and predicting such material behavior is of significant interest e.g. to support designs for crash or impact. Mg alloys exhibit complex strain-rate sensitive behavior owing to underlying deformation mechanisms (Ardeljan et al., 2016; Jahedi et al., 2018; Kabirian et al., 2015; Pandey et al., 2015; Zecevic et al., 2020). This paper is a contribution towards predicting the true visco-plastic properties of polycrystalline alloy AZ31 using T-CPFE, a multi-level constitutive model linking the grain-level to polycrystalline aggregate-level to FE macro-level material response.

The numerical method incorporated at the deformation mechanism-level facilitates the use of strain-rate sensitivity exponents corresponding to any value of strain-rate sensitivity. As a result, the true values of strain-rate sensitivity of deformation mechanisms were utilized in the T-CPFE simulations of AZ31. The use of accurate values of the constant structure strain-rate sensitivities allowed for accurate characterization of the strain-rate sensitive evolution of slip resistances, τ_c^s, which are governed by the thermally activated hardening law.

To demonstrate the utility of the developed T-CPFE model, a comprehensive dataset of alloy AZ31 collected over a wide range of strain-rates from 10^{-3} s^{-1} to 10^{3} s^{-1} is used. Over this range, a comparison between measured and predicted flow stress corresponding to a fixed microstructural states at 0.02 and 0.08 strains under tension and compression is performed. The plots consisted of comparing macroscopic stress versus strain-rate. In terms of the model, this could be thought of holding distributions of slip/twin resistances corresponding to the two microstructural states constant, while applying strain-rates. As shown, the model achieves good agreement because the appropriate values of the power-law exponents per slip/twin mode were used. These predictions of the strain-rate sensitive

Table 3
Adjusted values of strain-rate sensitivity per slip mode, m^α.

Parameter	Basal, $\alpha = 1$	Prismatic, $\alpha = 2$	Pyramidal, $\alpha = 3$
n^α	20	20	20
k^α	49999	1	3
$n^\alpha\ (k^\alpha + 1)$	1000000	40	80
m^α	0.000001	0.025	0.0125

response derive purely from the exponent.

Slip/twin resistances evolve with straining and are dependent on strain-rate. The hardening law for slip and twinning is calibrated using the flow stress and structure evolution data to govern the activation of deformation mechanisms. The in-plane (RD) flow stress in compression is accurately predicted as approximately strain-rate insensitive for the early portion of deformation as a result of the deformation dominated by basal slip and extension twinning. These predictions verify measurements that these two deformation mechanisms are strain-rate insensitive. As twins reorient texture in the material, pyramidal and prismatic slip mechanisms increasingly activate. As a result of strain-rate sensitivity of these slip mechanisms, the overall material exhibits increasingly strain-rate sensitive response. Under loading in tension, the alloy exhibits strong strain-rate sensitivity. Such behavior is a consequence of tensile deformation being accommodated primarily by slip and, in particular, prismatic slip. The increase in tension/compression asymmetry with strain-rate is also predicted well since it is a consequence of accurate modeling of strain-rate sensitivities intrinsic to the deformation mechanisms accommodating tension vs compression. The strain-rate sensitivity of the ND compression results primarily from pyramidal slip. As the compressive response in RD and ND are successfully predicted at strain-rates of $10^{-3}\ s^{-1}$ and $10^{3}\ s^{-1}$, the model also captures the evolution of anisotropy with strain-rate. More importantly, the increase in the rate of strain hardening with strain-rate is accurately predicted to be governed primarily by the evolution of slip/twin resistance. Note that the response in ND compression under $10^{3}\ s^{-1}$ strain-rate is stronger than under $10^{-3}\ s^{-1}$ not only because of strain-rate sensitivity of pyramidal slip system but also because of the rapid rate of hardening. Contraction twins induce this hardening, which is modeled using the barrier effect. The thin contraction twins are known to cause such hardening since they cut the path of the pyramidal dislocations (Knezevic et al., 2010).

We also show that the model can be used to refine measured strain-rate sensitivity per deformation mode by improving the fits of the flow stress experimental data relative to those achieved using the measured strain rate sensitivities. The fits are slightly improved by refining the strain-rate sensitivities associated with the slip modes and, in particular, by making the pyramidal slip a bit more strain-rate sensitive than in the measurements (Fig. 10, Table 3). In order to use the model to infer strain rate sensitivities inherent to deformation mechanisms, relative activities must be roughly known.

In closing, we note that the required power-law exponents to represent strain-rate sensitive behavior of materials are very large such that the non-linear scaling between the normalized shearing rate and the resolved shear stress normalized by the resistance is extraordinarily high. Such underlying hypothesis that the power-law behavior invokes can be circumvented by a more physics-based constitutive model relying on the Orowan's equation and transition state theory (Kothari and Anand, 1998). The equation of Orowan relates the slip system shear rates with a density of mobile dislocations and an average value of dislocation velocity (Orowan, 1940). The average dislocation velocity is defined in terms of the resolved shear stress, critical resolved shear stress, and temperature using the transition-state theory (Krausz and Eyring, 1975). Nevertheless, it is shown here that the widely used visco-plastic flow rule when appropriately modified, in combination with a physics-based dislocation density hardening law, can successfully predict a complex strain-rate dependent response of AZ31.

6. Conclusions

A numerical method enabling the use of true strain-rate sensitivity exponents for polycrystalline materials is implemented within a CPFE model. Importantly, the method does not increase computation time involved in simulations. The method facilitates separation of a strain-rate sensitivity embedded in the evolution of slip/twin resistances due to microstructural evolution and the constant structure strain-rate sensitivity driven by the exponent. The development presented in this paper marks the first time T-CPFE model implementation able to represent thermally activated dislocation glide per slip mode and twinning in a quantitative agreement with a wide range of strain-rate experimental conditions, without superfluous strain-rate effects entering numerically via the power-law exponent. The enhanced CPFE model is multi-level in nature, in which the grain-level to polycrystalline aggregate-level to FE macro-level modeling components, operate concurrently. In the model, resistances to slip/twin evolve as a function of strain-rate using a dislocation density-based hardening law. To demonstrate the utility of the enhanced CPFE, simulations are performed for alloy AZ31, which exhibits a variable strain-rate sensitivity of deformation mechanisms from relatively low, $m = 10^{-6}$ or equivalently the high exponent value of 10^{6}, to relatively high, $m = 0.025$ or equivalently the exponent value of 40. These simulations are the crystal visco-plasticity modeling of alloy AZ31 with the measured values of deformation mechanism strain-rate sensitivities governing the macro-level flow stress response to facilitate the quantitative verification over a wide range of experimental conditions. The model accurately predicts flow stress and evolution of texture and twinning for a broad range of strain-rates ranging from $10^{-3}\ s^{-1}$ to $10^{3}\ s^{-1}$ and loading orientations in tension and compression as a result of not only differing relative amounts of slip and twinning activity driven by a single set of accurately characterized hardening law parameters but also deformation mechanism-level strain-rate sensitivities. Calculations show that the model successfully captures the phenomena pertaining to the effect of increase in the strain-rate on the mechanical response including: (i) initially strain-rate independent followed by increasingly strain-rate dependent response with plastic strain for the in-plane compression, (ii) increasing rate of strain hardening with strain-rate for the through-thickness compression, (iii) constant strain-rate sensitivity under in-plane tension, and (iv) increasing tension/compression asymmetry with strain-rate. As the T-CPFE model successfully reproduces the mechanical data, it also validates the measured strain-rate dependency of deformation mechanisms. Hence, the model can also be used to verify and refine or infer strain-rate sensitivity per deformation mechanism by reproducing experimental data.

Declaration of competing interest

The authors declare that they have no known competing financial interests or personal relationships that could have appeared to influence the work reported in this paper.

Acknowledgements

This research was sponsored by the U.S. National Science Foundation and was accomplished under the CAREER grant no. CMMI-1650641. D.J.S. gratefully acknowledges discussions with Miroslav Zecevic about introducing the *k*-mod method into the T-CPFE framework and the Seaborg Institute for partial financial support under a post-doctoral fellowship through the Los Alamos National Laboratory LDRD program.

Appendix C. Supplementary data

Supplementary data to this article can be found online at https://doi.org/10.1016/j.ijplas.2021.103031.

Appendix A

This appendix summarizes equations pertaining to a strain-rate and temperature sensitive hardening law used in the present work for the evolution of resistances to slip/twin. The law is from (Ardeljan et al., 2016). Only the strain-rate effects are varied here and the temperature$T$ is taken to be 295 K. The law evolves resistance to slip using

$$\tau_c^s(\dot{\varepsilon}, T) = \tau_0^\alpha + \tau_{HP}^s + \tau_{for}^s(\dot{\varepsilon}, T) + \tau_{sub}^\alpha(\dot{\varepsilon}, T), \tag{A1}$$

where τ_0^α is the friction stress per slip mode α, τ_{HP}^s is the barrier (Hall-Petch (HP)-like) term evolving per slip system s due to twin lamellae since the grain size barrier effects is already embedded in τ_0^α, τ_{for}^s is a contribution to the evolution of slip resistance due to buildup of the forest dislocation density, and τ_{sub}^α is another evolving term due to the substructure/debris dislocation density.

The barrier term is

$$\tau_{HP}^s = \mu^\alpha H_i^\alpha \sqrt{\frac{b^\alpha}{d_{mfp}^s}}, \tag{A2}$$

where b^α is magnitude of the Burgers vector per mode α (3.21×10^{-10} m for basal, 3.21×10^{-10} m for prismatic, and 6.12×10^{-10} m for pyramidal), μ^α is the shear modulus (16,000 MPa for AZ31 (Watanabe et al., 2004)), H_i^α are the fitting HP parameters per slip mode for systems in grains having lamellae of either TTW ($i = 1$), or CTW ($i = 2$), or DTW ($i = 3$), and d_{mfp}^s is the mean-free-path for dislocations. The path is estimates as a distance between adjacent twin lamellae per grain using (Proust et al., 2007)

$$d_{mfp}^s = \frac{(1 - f^{pts})d_c}{\sin(\theta)}, \tag{A3}$$

where f^{pts} is the predominant twinning system (PTS) volume fraction, θ is the angle spanning between the given slip system and twin system planes, and d_c is the spacing estimated as the ratio between the average grain size, $d_g = 12\,\mu m$ for the studied AZ31, and the observed number of lamellae per grain (taken as 3). The model allows formation of multiple twin variants per grain, however, the PTS variant is used to estimate d_{mfp}^s.

The terms governed by the evolution of dislocation density populations, $\rho_{for}^s(\dot{\varepsilon}, T)$ and $\rho_{sub}(\dot{\varepsilon}, T)$, are (Madec et al., 2002)

$$\tau_{for}^s = b^\alpha \mu^\alpha \sqrt{\chi^{ss'} \rho_{for}^{s'}}, \quad \tau_{sub}^\alpha = 0.086 \mu^\alpha b^\alpha \sqrt{\rho_{sub}} log\left(\frac{1}{b^\alpha \sqrt{\rho_{sub}}}\right), \tag{A4}$$

in which $\chi^{ss'}$ is a matrix of dislocation interactions with the diagonal terms (s=s') set to 0.81 and the off-diagonal terms to zero (Lavrentev, 1980; Mecking and Kocks, 1981).

The first dislocation population evolves using (Essmann and Mughrabi, 1979; Mecking and Kocks, 1981)

$$\frac{\partial\rho^{s}_{for}}{\partial\gamma^{s'}}=\frac{\partial\rho^{s}_{gen,for}}{\partial\gamma^{s'}}-\frac{\partial\rho^{s}_{rem,for}}{\partial\gamma^{s'}}=k_1^{\alpha}\sqrt{\rho^{s}_{for}}-k_2^{s}(\dot{\varepsilon},T)\rho^{s}_{for},\quad \Delta\rho^{s}_{for}=\frac{\partial\rho^{s}_{for}}{\partial\gamma^{s'}}|\Delta\gamma^{s}|, \tag{A5}$$

where k_1^{α} is a fitting parameter for dislocation storage and $k_2^{\alpha}(\dot{\varepsilon},T)$ is a dynamic recovery parameter calculated based on the following law (Beyerlein and Tomé, 2008)

$$\frac{k_1^{\alpha}}{k_2^{s}(\dot{\varepsilon},T)}=\frac{1}{\sqrt{\left(\chi^{s's}\right)^{-1}\left(\frac{\tau^{\alpha}_{sat}}{b^{\alpha}\mu^{\alpha}}\right)^{2}}},\quad \tau^{\alpha}_{sat}=\frac{D^{\alpha}(b^{\alpha})^{3}g^{\alpha}\mu^{\alpha}}{\left(D^{\alpha}(b^{\alpha})^{3}-kTln\left(\frac{\dot{\varepsilon}}{\dot{\varepsilon}_0}\right)\right)}. \tag{A6}$$

Here, k, is the Boltzmann's constant, $\dot{\varepsilon}_0$ is a value of the reference value of strain-rate ($10^{7}\ \mathrm{s}^{-1}$), g^{α} is the activation enthalpy, and D^{α} is the drag stress. The second dislocation population increments using

$$\Delta\rho_{sub}=\sum_{s}q^{\alpha}b^{\alpha}\sqrt{\rho_{sub}}\ \frac{\partial\rho^{s}_{rem,for}}{\partial\gamma^{s'}}|\Delta\gamma^{s'}|, \tag{A7}$$

In which q^{α} is a fitting parameter for the amount of debris forming from the recovered dislocations.

The law evolves the resistance to twin using

$$\tau^{t}_{c}(\dot{\varepsilon},T)=\tau^{\beta}_{0}+\tau^{t}_{HP}+\tau^{\beta}_{slip}(\dot{\varepsilon},T). \tag{A8}$$

The friction term is

$$\tau^{\beta}_{0}=\tau^{\beta}_{prop}+\left(\tau^{\beta}_{crit}-\tau^{\beta}_{prop}\right)exp\left(-\sum_{s}\frac{\rho^{s}_{for}}{\rho^{s}_{sat}}\right), \tag{A9}$$

with the nucleation stress τ^{β}_{crit} and propagation stress τ^{β}_{prop}. The latter term is weighted by the probability term, $\rho^{s}_{sat}=\left(\frac{k_1^{\alpha}}{k_2^{s}}\right)^{2}$, which favors τ^{β}_{prop} over τ^{β}_{crit} with strain (Beyerlein and Tomé, 2008; Savage et al., 2021a). The HP barrier term is

$$\tau^{t}_{HP}=\frac{H^{\beta}_{0}}{\sqrt{d^{t}_{mfp}}}. \tag{A10}$$

Finally, the hardening term due to the slip and twin interactions is

$$\tau^{\beta}_{slip}=\mu^{\beta}\sum_{s}C^{\alpha\beta}b^{\beta}b^{\alpha}\rho^{s}_{for}. \tag{A11}$$

Here, $C^{\beta\alpha}$ is the interaction matrix and magnitudes of the Burgers vectors are 1.38×10^{-10} m for extension and 9.24×10^{-11} m for contraction twin modes. The crystal lattice reorientation associated with twinning is modeled using the composite grain (CG) model from (Proust et al., 2007) with the change that present model considers multiple twin variants as well as double twins per grain. Twin variants nucleate in grains when their fraction f^{t} reach a critical value, which is taken from a distribution centered at 5% for extension and 1% for contraction and double twins. Twin variants inherit parameters such as dislocation densities and slip/twin resistances from the parent grain upon nucleation. As a result of twin nucleation, the number of grains embedded at that FE integration points increases for the number of created twin variants. Growth/thickening of twins is facilitated by transfer of volume fraction from the parent grain to the variant with the shear strain accommodation.

Appendix B

The full form of the Jacobian modification to accommodate the k-mod is as follows

$$\frac{\partial\Delta\gamma^{s}_{k-\mathrm{mod}}}{\partial\mathbf{T}}=\Delta\gamma^{s}\frac{\partial|\mathbf{D}^{p,app}|^{\frac{k}{k+1}}}{\partial\mathbf{D}^{p,app}}\ \frac{\partial\mathbf{D}^{p,app}}{\partial\mathbf{T}}+|\mathbf{D}^{p,app}|^{\frac{k}{k+1}}\frac{\partial\Delta\gamma^{s}}{\partial\mathbf{T}} \tag{B1}$$

$$\frac{\partial\Delta\gamma^{s}_{k-\mathrm{mod}}}{\partial\mathbf{T}}=\Delta\gamma^{s}\frac{k}{k+1}|\mathbf{D}^{p,app}|^{\frac{-1}{k+1}}\frac{\mathbf{D}^{p,app}}{|\mathbf{D}^{p,app}|}\ \frac{\partial\mathbf{D}^{p,app}}{\partial\mathbf{T}}+|\mathbf{D}^{p,app}|^{\frac{k}{k+1}}\frac{\partial\Delta\gamma^{s}}{\partial\mathbf{T}} \tag{B2}$$

where $\frac{\partial\Delta\gamma^{s}}{\partial\mathbf{T}}$ is computed in the original model and $\frac{\partial\mathbf{D}^{p,app}}{\partial\mathbf{T}}$ is derived from Eq. (14) as

$$\frac{\partial\mathbf{D}^{p,app}}{\partial\mathbf{T}}\Delta t=\frac{\partial|\mathbf{D}^{p,app}|^{\frac{k}{k+1}}}{\partial\mathbf{D}^{p,app}}\ \frac{\partial\mathbf{D}^{p,app}}{\partial\mathbf{T}}\sum_{s}\Delta\gamma^{s}\mathbf{P}^{s}_{0}+|\mathbf{D}^{p,app}|^{\frac{k}{k+1}}\frac{\partial}{\partial\mathbf{T}}\left(\sum_{s}\Delta\gamma^{s}\mathbf{P}^{s}_{0}\right) \tag{B3}$$

$$\frac{\partial \mathbf{D}^{p,app}}{\partial \mathbf{T}}\Delta t = \frac{k}{k+1}|\mathbf{D}^{p,app}|^{\frac{-1}{k+1}}\frac{\mathbf{D}^{p,app}}{|\mathbf{D}^{p,app}|}\,\frac{\partial \mathbf{D}^{p,app}}{\partial \mathbf{T}}\sum_{s}\Delta\gamma^{s}\mathbf{P}_{0}^{s} + |\mathbf{D}^{p,app}|^{\frac{k}{k+1}}\sum_{s}\frac{\partial \Delta\gamma^{s}}{\partial \mathbf{T}}\mathbf{P}_{0}^{s} \tag{B4}$$

$$\frac{\partial \mathbf{D}^{p,app}}{\partial \mathbf{T}}\underbrace{\left[\mathbf{I}\Delta t - \frac{k}{k+1}\mathbf{D}^{p,app}|\mathbf{D}^{p,app}|^{-\frac{2+k}{k+1}}\sum_{s}\Delta\gamma^{s}\mathbf{P}_{0}^{s}\right]}_{\mathbf{A}} = |\mathbf{D}^{p,app}|^{\frac{k}{k+1}}\sum_{s}\frac{\partial \Delta\gamma^{s}}{\partial \mathbf{T}}\mathbf{P}_{0}^{s} \tag{B5}$$

$$\frac{\partial \mathbf{D}^{p,app}}{\partial \mathbf{T}} = \mathbf{A}^{-1}|\mathbf{D}^{p,app}|^{\frac{k}{k+1}}\sum_{s}\frac{\partial \Delta\gamma^{s}}{\partial \mathbf{T}}\mathbf{P}_{0}^{s} \tag{B6}$$

Author statement

William G. Feather.

Software, Validation, Formal analysis, Investigation, Visualization.

Daniel J. Savage.

Software, Validation, Investigation, Writing - Review & Editing.

Marko Knezevic.

Conceptualization, Methodology, Resources, Writing - Original Draft, Writing - Review & Editing, Supervision, Funding acquisition.

Declaration of competing InterestDoCI

The authors declare that they have no known competing financial interests or personal relationships that could have appeared to influence the work reported in this paper.

References

Akhtar, A., 1973. Compression of zirconium single crystals parallel to the c-axis. J. Nucl. Mater. 47, 79–86.
Akhtar, A., 1975. Prismatic slip in zirconium single crystals at elevated temperatures. MTA 6, 1217–1222.
Akhtar, A., Teghtsoonian, E., 1969. Solid solution strengthening of magnesium single crystals—I alloying behaviour in basal slip. Acta Metall. 17, 1339–1349.
Al-Samman, T., Gottstein, G., 2008. Room temperature formability of a magnesium AZ31 alloy: examining the role of texture on the deformation mechanisms. Mater. Sci. Eng., A 488, 406–414.
Alam, M.E., Pal, S., Decker, R., Ferreri, N.C., Knezevic, M., Beyerlein, I.J., 2020. Rare-earth- and aluminum-free, high strength dilute magnesium alloy for Biomedical Applications. Sci. Rep. 10, 15839.
Anand, L., 2004. Single-crystal elasto-viscoplasticity: application to texture evolution in polycrystalline metals at large strains. Comput. Methods Appl. Mech. Eng. 193, 5359–5383.
Anand, L., Kothari, M., 1996. A computational procedure for rate-independent crystal plasticity. J. Mech. Phys. Solid. 44, 525–558.
Ardeljan, M., Beyerlein, I.J., Knezevic, M., 2014. A dislocation density based crystal plasticity finite element model: application to a two-phase polycrystalline HCP/BCC composites. J. Mech. Phys. Solid. 66, 16–31.
Ardeljan, M., Beyerlein, I.J., Knezevic, M., 2017. Effect of dislocation density-twin interactions on twin growth in AZ31 as revealed by explicit crystal plasticity finite element modeling. Int. J. Plast. 99, 81–101.
Ardeljan, M., Beyerlein, I.J., McWilliams, B.A., Knezevic, M., 2016. Strain rate and temperature sensitive multi-level crystal plasticity model for large plastic deformation behavior: application to AZ31 magnesium alloy. Int. J. Plast. 83, 90–109.
Ardeljan, M., Knezevic, M., 2018. Explicit modeling of double twinning in AZ31 using crystal plasticity finite elements for predicting the mechanical fields for twin variant selection and fracture analyses. Acta Mater. 157, 339–354.
Ardeljan, M., Knezevic, M., Nizolek, T., Beyerlein, I.J., Mara, N.A., Pollock, T.M., 2015a. A study of microstructure-driven strain localizations in two-phase polycrystalline HCP/BCC composites using a multi-scale model. Int. J. Plast. 74, 35–57.
Ardeljan, M., McCabe, R.J., Beyerlein, I.J., Knezevic, M., 2015b. Explicit incorporation of deformation twins into crystal plasticity finite element models. Comput. Methods Appl. Mech. Eng. 295, 396–413.
Asaro, R.J., Needleman, A., 1985. Texture development and strain hardening in rate dependent polycrystals. Acta Metall. Mater. 33, 923–953.
Asgari, S., El-Danaf, E., Kalidindi, S.R., Doherty, R.D., 1997. Strain hardening regimes and microstructural evolution during large strain compression of low stacking fault energy fcc alloys that form deformation twins. Metall. Mater. Trans. A 28A, 1781–1795.
Barnett, M., 2003. A Taylor model based description of the proof stress of magnesium AZ31 during hot working. Metall. Mater. Trans. A 34, 1799–1806.
Barnett, M.R., 2007a. Twinning and the ductility of magnesium alloys: Part I: "Tension" twins. Mater. Sci. Eng., A 464, 1–7.
Barnett, M.R., 2007b. Twinning and the ductility of magnesium alloys: Part II. "Contraction" twins. Mater. Sci. Eng., A 464, 8–16.
Barnett, M.R., Keshavarz, Z., Beer, A.G., Atwell, D., 2004. Influence of grain size on the compressive deformation of wrought Mg–3Al–1Zn. Acta Mater. 52, 5093–5103.
Barrett, T.J., Knezevic, M., 2019. Deep drawing simulations using the finite element method embedding a multi-level crystal plasticity constitutive law: experimental verification and sensitivity analysis. Comput. Methods Appl. Mech. Eng. 354, 245–270.
Barrett, T.J., McCabe, R.J., Brown, D.W., Clausen, B., Vogel, S.C., Knezevic, M., 2020. Predicting deformation behavior of α-uranium during tension, compression, load reversal, rolling, and sheet forming using elasto-plastic, multi-level crystal plasticity coupled with finite elements. J. Mech. Phys. Solid. 138, 103924.
Barrett, T.J., Savage, D.J., Ardeljan, M., Knezevic, M., 2018. An automated procedure for geometry creation and finite element mesh generation: application to explicit grain structure models and machining distortion. Comput. Mater. Sci. 141, 269–281.
Basinski, Z.S., Szczerba, M.S., Niewczas, M., Embury, J.D., Basinski, S.J., 1997. Transformation of slip dislocations during twinning of copper-aluminum alloy crystals. Revue de Metallurgie. Cahiers D'Informations Techniques 94, 1037–1044.

Bathe, K.-J., 1996. Finite Element Procedures. Prentice Hall, Englewood Cliffs, N.J.
Becker, R., Lloyd, J.T., 2016. A reduced-order crystal model for HCP metals: application to Mg. Mech. Mater. 98, 98–110.
Beyerlein, I.J., Tomé, C.N., 2008. A dislocation-based constitutive law for pure Zr including temperature effects. Int. J. Plast. 24, 867–895.
Bouvier, S., Benmhenni, N., Tirry, W., Gregory, F., Nixon, M.E., Cazacu, O., Rabet, L., 2012. Hardening in relation with microstructure evolution of high purity α−titanium deformed under monotonic and cyclic simple shear loadings at room temperature. Mater. Sci. Eng., A 535, 12–21.
Chapuis, A., Liu, Q., 2019. Modeling strain rate sensitivity and high temperature deformation of Mg-3Al-1Zn alloy. Journal of Magnesium and Alloys 7, 433–443.
Chen, S., Gray, G., 1996. Constitutive behavior of tantalum and tantalum-tungsten alloys. Metall. Mater. Trans. A 27, 2994–3006.
Chun, Y.B., Davies, C.H.J., 2011. Twinning-induced negative strain rate sensitivity in wrought Mg alloy AZ31. Mater. Sci. Eng., A 528, 5713–5722.
Clausen, B., Tomé, C.N., Brown, D.W., Agnew, S.R., 2008. Reorientation and stress relaxation due to twinning: modeling and experimental characterization for Mg. Acta Mater. 56, 2456–2468.
Delannay, L., Kalidindi, S.R., Van Houtte, P., 2003. Quantitative prediction of textures in aluminium cold rolled to moderate strains (vol 336, pg 233, 2002). Mater. Sci. Eng.Struct. Mater.. Prop.Microstruct.Process 351, 358–359.
Diard, O., Leclercq, S., Rousselier, G., Cailletaud, G., 2005. Evaluation of finite element based analysis of 3D multicrystalline aggregates plasticity: application to crystal plasticity model identification and the study of stress and strain fields near grain boundaries. Int. J. Plast. 21, 691–722.
Duvvuru, H.K., Knezevic, M., Mishra, R.K., Kalidindi, S.R., 2007. Application of microstructure sensitive design to FCC polycrystals. Mater. Sci. Forum 546, 675–680.
Eghtesad, A., Germaschewski, K., Lebensohn, R.A., Knezevic, M., 2020. A multi-GPU implementation of a full-field crystal plasticity solver for efficient modeling of high-resolution microstructures. Comput. Phys. Commun. 107231.
Eghtesad, A., Knezevic, M., 2020. A full-field crystal plasticity model including the effects of precipitates: application to monotonic, load reversal, and low-cycle fatigue behavior of Inconel 718. Mater. Sci. Eng., A 140478.
El Kadiri, H., Oppedal, A.L., 2010. A crystal plasticity theory for latent hardening by glide twinning through dislocation transmutation and twin accommodation effects. J. Mech. Phys. Solid. 58, 613–624.
Essmann, U., Mughrabi, H., 1979. Annihilation of dislocations during tensile and cyclic deformation and limits of dislocation densities. Philos. Mag. A 40, 731–756.
Fast, T., Knezevic, M., Kalidindi, S.R., 2008. Application of microstructure sensitive design to structural components produced from hexagonal polycrystalline metals. Comput. Mater. Sci. 43, 374–383.
Feather, W.G., Ghorbanpour, S., Savage, D.J., Ardeljan, M., Jahedi, M., McWilliams, B.A., Gupta, N., Xiang, C., Vogel, S.C., Knezevic, M., 2019. Mechanical response, twinning, and texture evolution of WE43 magnesium-rare earth alloy as a function of strain rate: experiments and multi-level crystal plasticity modeling. Int. J. Plast. 120, 180–204.
Feng, Z., Zecevic, M., Knezevic, M., 2021. Stress-assisted (γ→α′) and strain-induced (γ→ε→α′) phase transformation kinetics laws implemented in a crystal plasticity model for predicting strain path sensitive deformation of austenitic steels. Int. J. Plast. 136, 102807.
Fernández, A., Jérusalem, A., Gutiérrez-Urrutia, I., Pérez-Prado, M.T., 2013. Three-dimensional investigation of grain boundary–twin interactions in a Mg AZ31 alloy by electron backscatter diffraction and continuum modeling. Acta Mater. 61, 7679–7692.
Follansbee, P., 1986. High-strain-rate Deformation of FCC Metals and Alloys, Metallurgical Applications of Shock-Wave and High-Strain-Rate Phenomena. Marcel Dekker, INC., New York, pp. 451–479.
Follansbee, P., Kocks, U., 1988. A constitutive description of the deformation of copper based on the use of the mechanical threshold stress as an internal state variable. Acta Metall. 36, 81–93.
Ghorbanpour, S., Alam, M.E., Ferreri, N.C., Kumar, A., McWilliams, B.A., Vogel, S.C., Bicknell, J., Beyerlein, I.J., Knezevic, M., 2020a. Experimental characterization and crystal plasticity modeling of anisotropy, tension-compression asymmetry, and texture evolution of additively manufactured Inconel 718 at room and elevated temperatures. Int. J. Plast. 125, 63–79.
Ghorbanpour, S., McWilliams, B.A., Knezevic, M., 2019a. Effect of hot working and aging heat treatments on monotonic, cyclic, and fatigue behavior of WE43 magnesium alloy. Mater. Sci. Eng., A 747, 27–41.
Ghorbanpour, S., McWilliams, B.A., Knezevic, M., 2019b. Low-cycle fatigue behavior of rolled WE43-T5 magnesium alloy. Fatig. Fract. Eng. Mater. Struct. 42, 1357–1372.
Ghorbanpour, S., McWilliams, B.A., Knezevic, M., 2020b. Effects of environmental temperature and sample pre-straining on high cycle fatigue strength of WE43-T5 magnesium alloy. Int. J. Fatig. 141, 105903.
Ghorbanpour, S., Zecevic, M., Kumar, A., Jahedi, M., Bicknell, J., Jorgensen, L., Beyerlein, I.J., Knezevic, M., 2017. A crystal plasticity model incorporating the effects of precipitates in superalloys: application to tensile, compressive, and cyclic deformation of Inconel 718. Int. J. Plast. 99, 162–185.
Hosford, W.F., 2010. Mechanical Behavior of Materials. Cambridge University Press, New York, NY, USA.
Hutchinson, J.W., 1976. Bounds and self-consistent estimates for creep of polycrystalline materials. In: Proceedings of the Royal Society of London. Series A, Mathematical and Physical Sciences, vol. 348, pp. 101–126.
Ishikawa, K., Watanabe, H., Mukai, T., 2005. High strain rate deformation behavior of an AZ91 magnesium alloy at elevated temperatures. Mater. Lett. 59, 1511–1515.
Jahedi, M., Ardeljan, M., Beyerlein, I.J., Paydar, M.H., Knezevic, M., 2015a. Enhancement of orientation gradients during simple shear deformation by application of simple compression. J. Appl. Phys. 117, 214309.
Jahedi, M., Knezevic, M., Paydar, M., 2015b. High-pressure double torsion as a severe plastic deformation process: experimental procedure and finite element modeling. J. Mater. Eng. Perform. 24, 1471–1482.
Jahedi, M., McWilliams, B.A., Kellogg, F.R., Beyerlein, I.J., Knezevic, M., 2018. Rate and temperature dependent deformation behavior of as-cast WE43 magnesium-rare earth alloy manufactured by direct-chill casting. Mater. Sci. Eng., A 712, 50–64.
Jahedi, M., McWilliams, B.A., Moy, P., Knezevic, M., 2017. Deformation twinning in rolled WE43-T5 rare earth magnesium alloy: influence on strain hardening and texture evolution. Acta Mater. 131, 221–232.
Jain, A., Agnew, S.R., 2007. Modeling the temperature dependent effect of twinning on the behavior of Mg alloy AZ31 sheet. Mater. Sci. Eng., A 29–36.
Kabirian, F., Khan, A.S., Gnäupel-Herlod, T., 2015. Visco-plastic modeling of mechanical responses and texture evolution in extruded AZ31 magnesium alloy for various loading conditions. Int. J. Plast. 68, 1–20.
Kalidindi, S.R., 1998. Incorporation of deformation twinning in crystal plasticity models. J. Mech. Phys. Solid. 46, 267–271.
Kalidindi, S.R., Bronkhorst, C.A., Anand, L., 1992. Crystallographic texture evolution in bulk deformation processing of FCC metals. J. Mech. Phys. Solid. 40, 537–569.
Kalidindi, S.R., Duvvuru, H.K., Knezevic, M., 2006. Spectral calibration of crystal plasticity models. Acta Mater. 54, 1795–1804.
Kaschner, G.C., Tomé, C.N., McCabe, R.J., Misra, A., Vogel, S.C., Brown, D.W., 2007. Exploring the dislocation/twin interactions in zirconium. Mater. Sci. Eng., A 463, 122–127.
Khan, A.S., Pandey, A., Gnäupel-Herold, T., Mishra, R.K., 2011. Mechanical response and texture evolution of AZ31 alloy at large strains for different strain rates and temperatures. Int. J. Plast. 27, 688–706.
Knezevic, M., Beyerlein, I.J., 2018. Multiscale modeling of microstructure-property relationships of polycrystalline metals during thermo-mechanical deformation. Adv. Eng. Mater. 20, 1700956.
Knezevic, M., Beyerlein, I.J., Brown, D.W., Sisneros, T.A., Tomé, C.N., 2013a. A polycrystal plasticity model for predicting mechanical response and texture evolution during strain-path changes: application to beryllium. Int. J. Plast. 49, 185–198.
Knezevic, M., Beyerlein, I.J., Lovato, M.L., Tomé, C.N., Richards, A.W., McCabe, R.J., 2014. A strain-rate and temperature dependent constitutive model for BCC metals incorporating non-Schmid effects: application to tantalum–tungsten alloys. Int. J. Plast. 62, 93–104.
Knezevic, M., Capolungo, L., Tomé, C.N., Lebensohn, R.A., Alexander, D.J., Mihaila, B., McCabe, R.J., 2012. Anisotropic stress-strain response and microstructure evolution of textured α-uranium. Acta Mater. 60, 702–715.
Knezevic, M., Daymond, M.R., Beyerlein, I.J., 2015. Modeling Discrete Twin Lamellae in a Microstructural Framework. Scripta Materialia (under review).
Knezevic, M., Daymond, M.R., Beyerlein, I.J., 2016a. Modeling discrete twin lamellae in a microstructural framework. Scripta Mater. 121, 84–88.

Knezevic, M., Ghorbanpour, S., Ferreri, N.C., Riyad, I.A., Kudzal, A.D., Paramore, J.D., Vogel, S.C., McWilliams, B.A., 2021. Thermo-hydrogen refinement of microstructure to improve mechanical properties of Ti–6Al–4V fabricated via laser powder bed fusion. Mater. Sci. Eng., A 809, 140980.

Knezevic, M., Kalidindi, S.R., 2007. Fast computation of first-order elastic-plastic closures for polycrystalline cubic-orthorhombic microstructures. Comput. Mater. Sci. 39, 643–648.

Knezevic, M., Lebensohn, R.A., Cazacu, O., Revil-Baudard, B., Proust, G., Vogel, S.C., Nixon, M.E., 2013b. Modeling bending of α-titanium with embedded polycrystal plasticity in implicit finite elements. Mater. Sci. Eng., A 564, 116–126.

Knezevic, M., Levinson, A., Harris, R., Mishra, R.K., Doherty, R.D., Kalidindi, S.R., 2010. Deformation twinning in AZ31: influence on strain hardening and texture evolution. Acta Mater. 58, 6230–6242.

Knezevic, M., McCabe, R.J., Lebensohn, R.A., Tomé, C.N., Liu, C., Lovato, M.L., Mihaila, B., 2013c. Integration of self-consistent polycrystal plasticity with dislocation density based hardening laws within an implicit finite element framework: application to low-symmetry metals. J. Mech. Phys. Solid. 61, 2034–2046.

Knezevic, M., McCabe, R.J., Tomé, C.N., Lebensohn, R.A., Chen, S.R., Cady, C.M., Gray Iii, G.T., Mihaila, B., 2013d. Modeling mechanical response and texture evolution of α-uranium as a function of strain rate and temperature using polycrystal plasticity. Int. J. Plast. 43, 70–84.

Knezevic, M., Zecevic, M., Beyerlein, I.J., Lebensohn, R.A., 2016b. A numerical procedure enabling accurate descriptions of strain rate-sensitive flow of polycrystals within crystal visco-plasticity theory. Comput. Methods Appl. Mech. Eng. 308, 468–482.

Kocks, U., Argon, A., Ashby, M., 1975. Thermodynamics and kinetics of slip. Prog. Mater. Sci. 19, 110–170.

Kocks, U.F., Tomé, C.N., Wenk, H.-R., 1998. Texture and Anisotropy. Cambridge University Press, Cambridge, UK.

Kok, S., Beaudoin, A.J., Tortorelli, D.A., 2002. A polycrystal plasticity model based on the mechanical threshold. Int. J. Plast. 18, 715–741.

Korla, R., Chokshi, A.H., 2010. Strain-rate sensitivity and microstructural evolution in a Mg–Al–Zn alloy. Scripta Mater. 63, 913–916.

Kothari, M., Anand, L., 1998. Elasto-viscoplastic constitutive equations for polycrystalline metals: application to tantalum. J. Mech. Phys. Solid. 46, 51–83.

Krausz, A.S., Eyring, H., 1975. Deformation Kinetics. Wiley.

Kumar, A.M., Kanjarla, A.K., Niezgoda, S.R., Lebensohn, R.A., Tomé, C.N., 2015. Numerical study of the stress state of a deformation twin in magnesium. Acta Mater. 84, 349–358.

Kurukuri, S., Worswick, M.J., Ghaffari Tari, D., Mishra, R.K., Carter, J.T., 2014. Rate sensitivity and tension–compression asymmetry in AZ31B magnesium alloy sheet. Phil. Trans. Math. Phys. Eng. Sci. 372, 20130216.

Landry, N., Knezevic, M., 2015. Delineation of first-order elastic property closures for hexagonal metals using fast fourier transforms. Materials 8, 6326–6345.

Lavrentev, F.F., 1980. The type of dislocation interaction as the factor determining work hardening. Mater. Sci. Eng. 46, 191–208.

Lebensohn, R.A., Kanjarla, A.K., Eisenlohr, P., 2012. An elasto-viscoplastic formulation based on fast Fourier transforms for the prediction of micromechanical fields in polycrystalline materials. Int. J. Plast. 32–33, 59–69.

Lebensohn, R.A., Tomé, C.N., 1993. A self-consistent anisotropic approach for the simulation of plastic deformation and texture development of polycrystals: application to zirconium alloys. Acta Metall. Mater. 41, 2611–2624.

Lentz, M., Klaus, M., Beyerlein, I.J., Zecevic, M., Reimers, W., Knezevic, M., 2015. In situ X-ray diffraction and crystal plasticity modeling of the deformation behavior of extruded Mg–Li–(Al) alloys: an uncommon tension–compression asymmetry. Acta Mater. 86, 254–268.

Li, H.W., Yang, H., Sun, Z.C., 2008. A robust integration algorithm for implementing rate dependent crystal plasticity into explicit finite element method. Int. J. Plast. 24, 267–288.

Lou, X.Y., Li, M., Boger, R.K., Agnew, S.R., Wagoner, R.H., 2007. Hardening evolution of AZ31B Mg sheet. Int. J. Plast. 23, 44–86.

Madec, R., Devincre, B., Kubin, L.P., 2002. From dislocation junctions to forest hardening. Phys. Rev. Lett. 89, 255508.

McGinty, R.D., McDowell, D.L., 2006. A semi-implicit integration scheme for rate independent finite crystal plasticity. Int. J. Plast. 22, 996–1025.

Mecking, H., Kocks, U.F., 1981. Kinetics of flow and strain-hardening. Acta Metall. Mater. 29, 1865–1875.

Molodov, K.D., Al-Samman, T., Molodov, D.A., 2017. Profuse slip transmission across twin boundaries in magnesium. Acta Mater. 124, 397–409.

Orowan, E., 1940. Problems of plastic gliding. Proc. Phys. Soc. 52, 8.

Pandey, A., Kabirian, F., Hwang, J.-H., Choi, S.-H., Khan, A.S., 2015. Mechanical responses and deformation mechanisms of an AZ31 Mg alloy sheet under dynamic and simple shear deformations. Int. J. Plast. 68, 111–131.

Paramatmuni, C., Kanjarla, A.K., 2019. A crystal plasticity FFT based study of deformation twinning, anisotropy and micromechanics in HCP materials: application to AZ31 alloy. Int. J. Plast. 113, 269–290.

Paramore, J.D., Fang, Z.Z., Sun, P., Koopman, M., Chandran, K.S.R., Dunstan, M., 2015. A powder metallurgy method for manufacturing Ti-6Al-4V with wrought-like microstructures and mechanical properties via hydrogen sintering and phase transformation (HSPT). Scripta Mater. 107, 103–106.

Partridge, P.G., 1967. The crystallography and deformation modes of hexagonal close-packed metals. Metallurgia Revised 12, 169.

Peirce, D., Asaro, R.J., Needleman, A., 1983. Material rate dependence and localized deformation in crystalline solids. Acta Metall. 31, 1951–1976.

Poulin, C.M., Korkolis, Y.P., Kinsey, B.L., Knezevic, M., 2019. Over five-times improved elongation-to-fracture of dual-phase 1180 steel by continuous-bending-under-tension. Mater. Des. 161, 95–105.

Proust, G., Tomé, C.N., Jain, A., Agnew, S.R., 2009a. Modeling the effect of twinning and detwinning during strain-path changes of magnesium alloy AZ31. Int. J. Plast. 25, 861–880.

Proust, G., Tomé, C.N., Jain, A., Agnew, S.R., 2009b. Modeling the effect of twinning and detwinning during strain path changes of Mg alloy AZ31. Int. J. Plast. 25, 861–880.

Proust, G., Tomé, C.N., Kaschner, G.C., 2007. Modeling texture, twinning and hardening evolution during deformation of hexagonal materials. Acta Mater. 55, 2137–2148.

Risse, M., Lentz, M., Fahrenson, C., Reimers, W., Knezevic, M., Beyerlein, I.J., 2017. Elevated temperature effects on the plastic anisotropy of an extruded Mg-4 Wt Pct Li alloy: experiments and polycrystal modeling. Metall. Mater. Trans. A 48, 446–458.

Riyad, I.A., Feather, W.G., Vasilev, E., Lebensohn, R.A., McWilliams, B.A., Pilchak, A.L., Knezevic, M., 2021. Modeling the role of local crystallographic correlations in microstructures of Ti-6Al-4V using a correlated structure visco-plastic self-consistent polycrystal plasticity formulation. Acta Mater. 203, 116502.

Savage, D.J., Cazacu, O., Knezevic, M., 2017. Dilational response of voided polycrystals. JOM 69, 942–947.

Savage, D.J., Feng, Z., Knezevic, M., 2021a. Identification of crystal plasticity model parameters by multi-objective optimization integrating microstructural evolution and mechanical data. Comput. Methods Appl. Mech. Eng. 379, 113747.

Savage, D.J., McCabe, R.J., Knezevic, M., 2021b. An automated procedure built on MTEX for reconstructing deformation twin hierarchies from electron backscattered diffraction datasets of heavily twinned microstructures. Mater. Char. 171, 110808.

Schmidt, J., Beyerlein, I.J., Knezevic, M., Reimers, W., 2021. Adjustment of the mechanical properties of Mg2Nd and Mg2Yb by optimizing their microstructures. Metals 11, 377.

Segurado, J., Lebensohn, R.A., Llorca, J., Tomé, C.N., 2012. Multiscale modeling of plasticity based on embedding the viscoplastic self-consistent formulation in implicit finite elements. Int. J. Plast. 28, 124–140.

Slutsky, L.J., Garland, C.W., 1957. Elastic constants of magnesium from 4.2 K to 300 K. Phys. Rev. 107, 972–976.

Song, S., Gray, G., 1995. Influence of temperature and strain rate on slip and twinning behavior of Zr. Metall. Mater. Trans. A 26, 2665–2675.

Song, S.G., Gray, I., T, G., 1995. Structural interpretation of the nucleation and growth of deformation twins in Zr and Ti–II. Tem study of twin morphology and defect reactions during twinning. Acta Metall. Mater. 43, 2339–2350.

Staroselsky, A., Anand, L., 2003. A constitutive model for hcp materials deforming by slip and twinning: application to magnesium alloy AZ31B. Int. J. Plast. 19, 1843–1864.

Tam, K.J., Vaughan, M.W., Shen, L., Knezevic, M., Karaman, I., Proust, G., 2020. Modelling the temperature and texture effects on the deformation mechanisms of magnesium alloy AZ31. Int. J. Mech. Sci. 182, 105727.

Tomé, C.N., 1999. Self-consistent polycrystal models: a directional compliance criterion to describe grain interactions. Model. Simulat. Mater. Sci. Eng. 7, 723–738.

Tomé, C.N., Lebensohn, R.A., Kocks, U.F., 1991. A model for texture development dominated by deformation twinning: application to zirconium alloys. Acta Metall. Mater. 39, 2667–2680.

Ulacia, I., Dudamell, N.V., Gálvez, F., Yi, S., Pérez-Prado, M.T., Hurtado, I., 2010. Mechanical behavior and microstructural evolution of a Mg AZ31 sheet at dynamic strain rates. Acta Mater. 58, 2988–2998.

Van Houtte, P., 1978. Simulation of the rolling and shear texture of brass by the Taylor theory adapted for mechanical twinning. Acta Metall. Mater. 26, 591–604.

Wang, H., Wu, P., Kurukuri, S., Worswick, M.J., Peng, Y., Tang, D., Li, D., 2018. Strain rate sensitivities of deformation mechanisms in magnesium alloys. Int. J. Plast. 107, 207–222.

Wang, J., Zhu, G., Wang, L., Vasilev, E., Park, J.-S., Sha, G., Zeng, X., Knezevic, M., 2021. Origins of high ductility exhibited by an extruded magnesium alloy Mg-1.8Zn-0.2Ca: experiments and crystal plasticity modeling. J. Mater. Sci. Technol. 84, 27–42.

Watanabe, H., Ishikawa, K., 2009. Effect of texture on high temperature deformation behavior at high strain rates in a Mg–3Al–1Zn alloy. Mater. Sci. Eng., A 523, 304–311.

Watanabe, H., Mukai, T., Sugioka, M., Ishikawa, K., 2004. Elastic and damping properties from room temperature to 673 K in an AZ31 magnesium alloy. Scripta Mater. 51, 291–295.

Wu, X., Kalidindi, S.R., Necker, C., Salem, A.A., 2007a. Prediction of crystallographic texture evolution and anisotropic stress-strain curves during large plastic strains in high purity α-titanium using a Taylor-type crystal plasticity model. Acta Mater. 55, 423–432.

Wu, X., Proust, G., Knezevic, M., Kalidindi, S.R., 2007b. Elastic-plastic property closures for hexagonal close-packed polycrystalline metals using first-order bounding theories. Acta Mater. 55, 2729–2737.

Yoo, M.H., 1981. Slip, twinning, and fracture in hexagonal close-packed metals. Metall. Mater. Trans. A 12, 409–418.

Yuan, W., Panigrahi, S.K., Su, J.Q., Mishra, R.S., 2011. Influence of grain size and texture on Hall–Petch relationship for a magnesium alloy. Scripta Mater. 65, 994–997.

Zecevic, M., Beyerlein, I.J., Knezevic, M., 2017. Coupling elasto-plastic self-consistent crystal plasticity and implicit finite elements: applications to compression, cyclic tension-compression, and bending to large strains. Int. J. Plast. 93, 187–211.

Zecevic, M., Beyerlein, I.J., McCabe, R.J., McWilliams, B.A., Knezevic, M., 2016a. Transitioning rate sensitivities across multiple length scales: microstructure-property relationships in the Taylor cylinder impact test on zirconium. Int. J. Plast. 84, 138–159.

Zecevic, M., Knezevic, M., 2015. A dislocation density based elasto-plastic self-consistent model for the prediction of cyclic deformation: application to Al6022-T4. Int. J. Plast. 72, 200–217.

Zecevic, M., Knezevic, M., 2017. Modeling of sheet metal forming based on implicit embedding of the elasto-plastic self-consistent formulation in shell elements: application to Cup drawing of AA6022-T4. JOM 69, 922–929.

Zecevic, M., Knezevic, M., 2018. Latent hardening within the elasto-plastic self-consistent polycrystal homogenization to enable the prediction of anisotropy of AA6022-T4 sheets. Int. J. Plast. 105, 141–163.

Zecevic, M., Knezevic, M., 2019. An implicit formulation of the elasto-plastic self-consistent polycrystal plasticity model and its implementation in implicit finite elements. Mech. Mater. 136, 103065.

Zecevic, M., Knezevic, M., McWilliams, B., Lebensohn, R.A., 2020. Modeling of the thermo-mechanical response and texture evolution of WE43 Mg alloy in the dynamic recrystallization regime using a viscoplastic self-consistent formulation. Int. J. Plast. 130, 102705.

Zecevic, M., Korkolis, Y.P., Kuwabara, T., Knezevic, M., 2016b. Dual-phase steel sheets under cyclic tension–compression to large strains: experiments and crystal plasticity modeling. J. Mech. Phys. Solid. 96, 65–87.

Zecevic, M., McCabe, R.J., Knezevic, M., 2015a. A new implementation of the spectral crystal plasticity framework in implicit finite elements. Mech. Mater. 84, 114–126.

Zecevic, M., McCabe, R.J., Knezevic, M., 2015b. Spectral database solutions to elasto-viscoplasticity within finite elements: application to a cobalt-based FCC superalloy. Int. J. Plast. 70, 151–165.